

---

# Merging Memory and Space: A Spatiotemporal State Space Neural Operator

---

**Nodens F. Koren**

Department of Computer Science  
ETH Zürich  
nodens.koren@inf.ethz.ch

**Samuel Lanthaler**

Faculty of Mathematics  
University of Vienna  
samuel.lanthaler@univie.ac.at

## Abstract

We propose the *Spatiotemporal State Space Neural Operator* (ST-SSM), a compact architecture for learning solution operators of time-dependent partial differential equations (PDEs). ST-SSM introduces a novel factorization of the spatial and temporal dimensions, using structured state-space models to independently model temporal evolution and spatial interactions. This design enables parameter efficiency and flexible modeling of long-range spatiotemporal dynamics. A theoretical connection is established between SSMs and neural operators, and a unified universality theorem is proved for the resulting class of architectures. Empirically, we demonstrate that our factorized formulation outperforms alternative schemes such as zigzag scanning and parallel independent processing on several PDE benchmarks, including 1D Burgers’ equation, 1D Kuramoto–Sivashinsky Equation, and 2D Navier–Stokes equations under varying physical conditions. Our model performs competitively with existing baselines while using significantly fewer parameters. In addition, our results reinforce previous findings on the benefits of temporal memory by showing improved performance under partial observability. Our results highlight the advantages of dimensionally factorized operator learning for efficient and generalizable PDE modeling, and put this approach on a firm theoretical footing.

## 1 Introduction

Many problems in scientific computing require approximating a nonlinear operator that maps input functions to output functions, often governed by an underlying system of partial differential equations (PDEs). Neural operators (NOs) [14] have emerged as powerful models for this setting, offering a mesh-independent framework that operates directly on functions and generalizes across discretizations. Among these, the Fourier Neural Operator (FNO) [20] effectively leverages global convolution kernels in the Fourier domain to model long-range spatial correlations. However, the fully global nature of FNO comes with substantial computational cost, especially for higher-dimensional PDEs.

To address this, factorized variants of FNO have been proposed that decompose the operator learning problem into lower-dimensional subspaces [28, 18, 19]. These light-weight formulations retain much of FNO’s modeling capacity while offering better efficiency, especially in high-dimensional settings. Meanwhile, advances in state space models (SSMs) [9], including the diagonal version of the Structured State Space (S4D) architecture [8], have shown remarkable success in processing long-range temporal dependencies with linear time and memory complexity.

In this work, we are motivated by the need for accurate and scalable operator learning models in higher-dimensional spatiotemporal problems. We introduce the Spatio-Temporal Structured State Space Model (ST-SSM), which applies SSMs directly over the joint spatiotemporal domain. This approach can be interpreted in two complementary ways: as an extension of SSMs from purely temporal

modeling to full spatiotemporal operator learning, or alternatively, as an adaptive generalization of the FNO architecture. In contrast to FNO’s fixed global filters, ST-SSM learns adaptive convolutional kernels whose receptive fields and frequency content are learned from data.

Theoretically, we establish a foundational result on the universality of operator learning with convolutional kernels: any continuous operator can be approximated arbitrarily well using convolutional NOs, provided that the architecture has a full field-of-view over its input. This intuitive requirement—formally proved here—is satisfied by both FNO and ST-SSM. As a crucial distinction, we show that the spatial-only variant of ST-SSM subsumes factorized FNO as a special case, while introducing two additional degrees of adaptivity: localized receptive fields (via damping) and mode selection (via frequency modulation). Moreover, the temporal component of ST-SSM naturally enforces causality, a desirable inductive bias for many time-evolving PDEs.

Taken together, these properties give ST-SSM a strong theoretical grounding as a parameter-efficient and flexible architecture for operator learning. Our numerical experiments on 1D and 2D benchmarks—ranging from chaotic dynamics in the Kuramoto–Sivashinsky equation to long-time evolution in 2D Navier–Stokes flows—demonstrate that these theoretical benefits also translate to practical gains. Across the board, ST-SSM matches or exceeds the performance of existing baselines while using significantly fewer parameters and requiring less memory. This makes it a promising tool for advancing data-driven modeling in engineering and the physical sciences.

## 2 Related Work

### 2.1 Neural Operators

Data-driven neural operators have emerged as a powerful framework for learning PDE solution operators [5, 1, 23, 14]. Theoretical work established that several neural operators can universally approximate nonlinear operators [5, 13, 15, 17], including DeepONet [23, 16] and the Fourier Neural Operator (FNO), which implements global convolution via the Fourier transform [20]. Extensions such as the Factorized Fourier Neural Operator (FFNO) [28] enhance efficiency and expressivity in practice, but their theoretical expressivity remains unknown. Alternative inductive biases have also been explored, including U-Net–based convolutional operators [26, 10, 25, 27] and attention-based operators like the Galerkin Transformer (GKT) [4].

While some studies suggest that purely Markovian models can be performant for learning time-evolution PDEs [28, 22], recent work has begun to integrate memory mechanisms into neural operators. For example, Buitrago et al. [3] introduce the Memory Neural Operator (MemNO), which embeds an S4-based structured recurrence module within an FNO backbone, motivated by the Mori–Zwanzig formalism [24, 31]. It is found that incorporating past states can significantly improve the accuracy of time-dependent PDE predictions, especially under low-resolution or noisy conditions. Our work builds on this insight by examining scenarios with missing contextual information and by introducing a spatiotemporal factorization that distributes memory across *both time and space*.

### 2.2 Structured State Space Models (SSMs)

Structured state space models (SSMs) have recently achieved strong results on long-range sequence tasks in natural language processing and vision. The Structured State Space sequence model (S4) [9, 8] use a continuous-time linear SSM layer to capture very long-range dependencies efficiently, and the Mamba model [7] extends this idea by making the SSM parameters input-dependent, further improving performance on large-scale language modeling tasks. These SSM-based architectures have been shown to match or exceed Transformer performance on a variety of benchmark tasks.

SSMs have also begun to be used in operator learning. For example, Hu et al. [12] incorporate Mamba-style SSM layers to predict dynamical systems efficiently. In the context of neural PDE solvers, recent works like Cheng et al. [6] and Zheng et al. [29] embed Mamba SSM modules to capture spatial correlations in solution fields. These methods primarily focus on spatial modeling, applying SSM layers across spatial dimensions or treating time steps sequentially. By contrast, our work focuses on applying SSMs jointly in both space and time, employing a unified spatiotemporal SSM architecture for neural operator learning.

### 3 Methodology

#### 3.1 Problem Formulation

Let  $\Omega \subset \mathbb{R}^d$  be a bounded spatial domain, and consider the solution  $u \in C([0, T]; L^2(\Omega; \mathbb{R}^V))$  of a time-dependent partial differential equation (PDE). We assume access to a dataset of  $N$  solution trajectories  $\{u^{(i)}(t, x)\}_{i=1}^N$  generated from varying initial or parametric conditions.

In practice, we discretize the spatial domain  $\Omega$  using an equispaced grid  $\mathcal{S}$  of resolution  $f$ , and the temporal domain  $[0, T]$  using an equispaced grid  $\mathcal{T}$  consisting of  $N_t + 1$  points. Let  $T_{\text{in}} < T$  denote a fixed input time horizon.

Given access to the trajectory segment  $u(t, x)|_{t \in [0, T_{\text{in}}]}$  on the spatial grid  $\mathcal{S}$ , our goal is to predict the full future evolution  $u(t, x)|_{t \in [T_{\text{in}}, T]}$  on the same spatial grid. That is, rather than forecasting a single future timestep given a past history, we aim to learn a model of the entire system dynamics conditioned on an initial segment of the trajectory. Formally, our NO model defines a parametric map  $\Psi_\theta : C(\mathcal{T}_{\text{in}}; L^2(\Omega; \mathbb{R}^V)) \rightarrow C(\mathcal{T}_{\text{out}}; L^2(\Omega; \mathbb{R}^V))$ , where  $\mathcal{T}_{\text{in}} = [0, T_{\text{in}}]$  and  $\mathcal{T}_{\text{out}} = [T_{\text{in}}, T]$ , that maps the input trajectory segment to the predicted future solution.

#### 3.2 Structured State Space Models (S4 and S4D)

We begin with the continuous-time linear state space model (SSM) defined as:

$$\begin{aligned} \frac{d}{dt}v(t) &= Av(t) + Bu(t), \\ y(t) &= Cv(t) + Du(t), \end{aligned} \quad (1)$$

where  $v(t) \in \mathbb{R}^N$  is the hidden state,  $u(t) \in \mathbb{R}$  is the input, and  $y(t) \in \mathbb{R}$  is the output. The matrices  $A \in \mathbb{R}^{N \times N}$ ,  $B \in \mathbb{R}^{N \times 1}$ ,  $C \in \mathbb{R}^{1 \times N}$ , and  $D \in \mathbb{R}$  define the system dynamics.

The Structured State Space (S4) model [9] introduces a parameterization where  $A$  is structured to allow efficient computation of the convolution kernel  $\kappa(t)$  corresponding to the system's impulse response. Specifically, S4 utilizes a diagonal plus low-rank (DPLR) structure,  $A = \Lambda + PQ^\top$ , where  $\Lambda \in \mathbb{C}^{N \times N}$  is diagonal, and  $P, Q \in \mathbb{C}^{N \times r}$  with  $r \ll N$ . This structure enables computation of  $\kappa(t)$  via the Cauchy kernel and allows for efficient implementation with the Fast Fourier Transform (FFT).

To further simplify the model, S4D [8] restricts  $A$  to be diagonal, i.e.,  $A = \text{diag}(\lambda_1, \dots, \lambda_N)$ , and initializes the eigenvalues  $\{\lambda_i\}$  to approximate the behavior of the original S4 model. This diagonalization reduces the computational complexity and memory footprint while retaining the ability to model long-range dependencies.

In both S4 and S4D, after computing the convolution with the kernel  $\kappa(t)$ , a pointwise nonlinearity  $\sigma(\cdot)$  (e.g., GELU) is applied, followed by a residual connection.

#### 3.3 Markovian Spatial State Space Model

To model spatial dependencies in PDEs, we extend the S4D framework to spatial dimensions. For a 1D spatial domain discretized into  $X$  points, we define two separate SSMs: a forward model  $\mathcal{M}_{\text{fwd}}$  and a backward model  $\mathcal{M}_{\text{bwd}}$ . Given an input sequence  $u \in \mathbb{R}^{X \times d}$ , the forward pass is computed as:

$$y_{\text{fwd}} = \mathcal{M}_{\text{fwd}}(u),$$

and the backward pass involves reversing the input sequence:

$$y_{\text{bwd}} = \text{flip}(\mathcal{M}_{\text{bwd}}(\text{flip}(u))),$$

where  $\text{flip}(\cdot)$  denotes reversing the sequence along the spatial dimension. The final output is the sum of the forward and backward passes:  $y = y_{\text{fwd}} + y_{\text{bwd}}$ .

For multi-dimensional spatial data, such as 2D grids with dimensions  $X \times Y$ , we apply this bidirectional processing sequentially along each spatial axis. Let  $u \in \mathbb{R}^{X \times Y \times d}$  be the input tensor. We first process along the  $x$ -axis:

$$u^{(x)} = u_{\text{fwd}}^{(x)} + u_{\text{bwd}}^{(x)}, \quad \begin{cases} u_{\text{fwd}}^{(x)} = \mathcal{M}_{\text{fwd}}^{(x)}(u), \\ u_{\text{bwd}}^{(x)} = \text{flip}_x(\mathcal{M}_{\text{bwd}}^{(x)}(\text{flip}_x(u))), \end{cases}$$

where  $\text{flip}_x(\cdot)$  denotes reversing along the  $x$ -axis. Then, we process along the  $y$ -axis:

$$y = u_{\text{fwd}}^{(y)} + u_{\text{bwd}}^{(y)}, \quad \begin{cases} u_{\text{fwd}}^{(y)} = \mathcal{M}_{\text{fwd}}^{(y)}(u^{(x)}), \\ u_{\text{bwd}}^{(y)} = \text{flip}_y \left( \mathcal{M}_{\text{bwd}}^{(y)}(\text{flip}_y(u^{(x)})) \right), \end{cases}$$

where  $\text{flip}_y(\cdot)$  denotes reversing along the  $y$ -axis. This sequential application of bidirectional SSMs along each spatial dimension allows the model to capture complex spatial dependencies while maintaining computational efficiency. We include a schematic of the model architecture in Appendix B.

**Comparison with Existing Methods.** Unlike Vision Mamba [30], which processes 2D data in a zigzag manner using bidirectional SSMs, our approach applies SSMs separately along each spatial dimension. Additionally, while Factorized Fourier Neural Operators (F-FNO) [28] process each spatial dimension in parallel and sum the results, our method applies SSMs sequentially, allowing for more expressive modeling of spatial interactions. Due to memory constraints on our available hardware, we do not employ Mamba-based SSMs directly but explore different configurations of 2D and factorized spatial SSMs using S4D in Appendix D.

### 3.4 Full Model: Incorporating Temporal Memory

To capture temporal dependencies, especially in time-dependent PDEs, we incorporate a non-Markovian temporal S4D block inspired by the Memory Neural Operator (MemNO) architecture [3]. The final ST-SSM architecture is a factorized architecture composed of two types of blocks: ordinary temporal S4D layers (memory layers) and the novel spatial SSM layers introduced in the last section. For our numerical experiments, we alternate (2x spatial)–(1x temporal)–(2x spatial) layers, leading to

$$\Psi_\theta = \mathcal{Q} \circ \mathcal{L}_4 \circ \mathcal{L}_3 \circ \mathcal{M} \circ \mathcal{L}_2 \circ \mathcal{L}_1 \circ \mathcal{R},$$

where  $\mathcal{R}$  and  $\mathcal{Q}$  are additional input and output lifting/projection acting only on the channel dimension,  $\mathcal{L}_j$  are spatial layers, and  $\mathcal{M}$  is a temporal memory module that aggregates information from previous timesteps. The memory layer  $\mathcal{M}$  has an internal state  $v_t^* = v^*(t, x) \in \mathbb{R}^H$ , depending on the whole input sequence  $u_{t-1}, u_{t-2}, \dots, u_0$ , and is updated over time by solving the state-space ODE (1).

Given a new input  $u_t$  and the current hidden state  $v_t^*$ , the output  $\Psi_{\theta, t+1}$  at the next time-step can be written as  $\Psi_{\theta, t+1} = \Psi_{\theta, t+1}(u_t, v_t^*)$ , where  $v_t^*$  is implicit in  $\mathcal{M}$ . When running inference, starting from known values  $u_0, \dots, u_{T_{in}}$ , we update the hidden state  $v_t^*$  up to time  $v_{T_{in}}^*$ , and then iteratively generate the model prediction  $u_{t+1} := \Psi_{\theta, t+1}(u_t, v_t^*)$  from previous  $u_t$  and  $v_t^*$  and update  $v_t^* \mapsto v_{t+1}^*$ . Memory from all past states is incorporated via  $v_t^*$ . This design allows the model to utilize information from the entire history of the system’s evolution, enhancing its ability to model complex temporal dynamics and improving robustness to noise and low-resolution inputs. In practice the number and placement of spatial and temporal layers can be tuned for specific applications.

## 4 Theory

We view the proposed ST-SSM architecture as an instance of a popular neural operator paradigm [14], combining two types of layers: (a) pointwise composition with nonlinear activations, and (b) application of nonlocal convolution operators, and with prototypical hidden layers of the form,

$$\mathcal{L} : v(x) \mapsto \underbrace{\sigma(Wv(x) + b)}_{\text{(a) nonlinear}} + \underbrace{\int_D \kappa(x - y)v(y) dy}_{\text{(b) nonlocal}}, \quad (2)$$

where  $v : D \rightarrow \mathbb{R}^H$  is a hidden state,  $\sigma$  is a standard activation function (e.g., GELU),  $W \in \mathbb{R}^{H \times H}$  is a weight matrix,  $b \in \mathbb{R}^H$  a bias vector and  $\kappa : D \rightarrow \mathbb{R}^{H \times H}$  is a learnable integral-kernel.

To give a unified discussion, we will say that  $\Psi$  is a **convolutional NO**, if it is of the form  $\Psi(u) = \mathcal{Q} \circ \mathcal{L}_L \circ \dots \circ \mathcal{L}_1 \circ \mathcal{R}(u)$ , with hidden layers  $\mathcal{L}_\ell$  as in (2), and choice of parametrized kernel  $\kappa_\ell(x) = \kappa_\ell(x; \theta)$ . In addition, we have a lifting layer  $\mathcal{R}(u)(x) := R(u(x), x)$  and projection layer  $\mathcal{Q}(v(x)) = Q(v(x))$  by composition with shallow neural networks  $R, Q$ . We next discuss three architectures exemplifying this approach, highlighting their commonality and giving a unified description. This results in a sharp *criterion for universality* for any such convolutional NO architecture.

**Fourier neural operator (FNO).** The FNO parametrizes the convolution kernel by a truncated Fourier series,  $\kappa(x) = \sum_{|k|_\infty \leq K} \hat{\kappa}_k e^{ikx}$ , with cut-off parameter  $K$ , and  $|k|_\infty = \max_{j=1, \dots, d} |k_j|$ .

The Fourier coefficients  $\hat{\kappa}_k \in \mathbb{C}^{H \times H}$  are complex-valued matrices. The parametrization of the integral kernel  $\kappa(x)$  of FNO in  $d$  dimensions entails a considerable memory footprint, requiring  $O(LH^2K^d)$  parameters. This can render FNO prohibitive in high-dimensional applications.

**Factorized FNO (F-FNO).** To lessen the computational demands of FNO, so-called ‘‘factorized’’ architectures have been introduced. Here, convolutions are taken along one dimension at a time. Mathematically, this corresponds to choosing kernels of the form  $\kappa(x) = \kappa_s(x_j) \prod_{k \neq j} \delta(x_k)$ , where  $\kappa_s(x_j)$  is a 1d FNO kernel and  $\delta(x_k)$  the Dirac delta function. Thus, integration is effectively only performed with respect to  $x_j$ . The resulting F-FNO only requires  $O(LH^2Kd)$  parameters [28].

**Spatial SSM.** We next consider the spatial convolution layers of the proposed ST-SSM architecture. In this case, solution of the ODE system (1) leads to an explicit formula for the corresponding kernel. For a 1d spatial domain, this results in a kernel  $\kappa(x) = \kappa_+(x) + \kappa_-(x)$ , where  $\kappa_{\pm}(x)$  correspond to the backward and forward scans, respectively, and  $\kappa_{\pm}(x)$  is of the form

$$\kappa_{\pm}(x) = 1_{\mathbb{R}_{\pm}}(x) \sum_{k=1}^K e^{r_k|x|} e^{i\omega_k x} C_k B_k^T, \quad r_k = \text{Real}(\lambda_k), \quad \omega_k = \text{Imag}(\lambda_k), \quad B_k, C_k \in \mathbb{R}^H. \quad (3)$$

Here  $1_{\mathbb{R}_{\pm}}(x)$  is the indicator function of  $\mathbb{R}_{\pm} = \{\pm x \geq 0\}$ . The main difference with FNO lies in the parametrization of the convolutional kernel  $\kappa$ , which now has tunable frequency parameters  $\omega_k \in \mathbb{R}$ , and tunable damping parameters  $r_k < 0$ . The parameter count of the resulting factorized spatial SSM architecture in  $d$ -dimensions requires at most  $O(LH(H+K)d)$  parameters.

A comparison of the model parameter count entailed by the above choices is summarized below:

Model	FNO	F-FNO	spatial-SSM
# Parameter (scaling)	$LH^2K^d$	$LH^2Kd$	$L(H^2 + HK)d$

#### 4.1 A Sharp Criterion for Universality of Convolutional NOs.

As highlighted above, FNO, factorized FNO and SSMs all share a common structure, distinguished by the chosen kernel parametrization. *What can be said about the expressivity of such architectures?* Our first goal is to derive a sharp, general condition for the universality of such convolutional NO architectures.

A minimal requirement for the universality of any neural network architecture is that the value of each output pixel must be informed by the values of *all* input pixels, i.e. the model needs to have a ‘‘full field of view’’. In the context of convolutional NO architectures, this leads to the following definition:

**Definition.** A convolutional NO architecture with layer kernels  $\kappa_1, \dots, \kappa_L$  has a **full field of view**, if the iterated kernel  $\bar{\kappa} := \kappa_L * \kappa_{L-1} * \dots * \kappa_1$  is non-vanishing, i.e.  $\bar{\kappa}(x - y) \neq 0$  for all  $x, y \in D$ .

The next result shows that this necessary condition is actually already sufficient for the universality of a convolutional architecture, requiring no additional assumptions on the convolution operators:

**Theorem 4.1.** A (factorized) convolutional NO architecture is universal if it has a full field of view.

We refer to Appendix A for the precise statement and proof. To the best of our knowledge, the criterion identified above is both the simplest and most widely applicable result for convolutional NO architectures; it implies universality of (vanilla) FNO, factorized FNOs and combinations of (F-)FNO and SSMs, ST-SSM and even gives a sharp criterion for the universality of *localized* convolutional NOs (similar to the CNO [26]), for which  $\kappa_{\ell}$  has localized support. A theoretical basis for both factorized and localized architectures had been missing from the literature. The above result closes this gap. Appendix C.1 contrasts empirical results with a unidirectional SSM that violates the criterion.

#### 4.2 Adaptivity and Enhanced Model Expressivity of ST-SSM

From the formula (3) it is evident that (factorized) spatial SSM is able to exactly recover FNO (in 1d), or F-FNO. In fact, it can represent any 1d convolutional kernel of the form

$$\kappa(x) = \sum_{k=1}^K c_k e^{-\rho_k|x|} e^{i\omega_k x}, \quad \rho_k \geq 0, \quad \omega_k \in \mathbb{R}. \quad (4)$$

When restricting this choice to  $\rho_k = 0$  and  $\omega_k = k$ , we recover the FNO kernel parametrization. However, since the damping and frequency are *tunable parameters* within ST-SSM, this adds further adaptivity: (1) choice of  $\rho_k > 0$  allows effective *kernel localization*; the model can optimize the support of its convolutional kernel, interpolating between the global kernels of FNO ( $\rho_k \approx 0$ ) and very localized CNN-like kernels ( $\rho_k \gg 1$ ). (2) additional adaptivity comes from *adaptive mode-filtering*; the model can optimize the frequencies  $\omega_1, \dots, \omega_K$ , most relevant for nonlocal processing. Thus, in theory, this added adaptivity implies enhanced model expressivity of ST-SSM over F-FNO.

## 5 Experiment Setup

### 5.1 Setup and Dataset Description

We evaluate our models on a suite of one-dimensional (1D) and two-dimensional (2D) partial differential equation (PDE) benchmarks commonly used in operator learning. These datasets span a variety of dynamical regimes—from chaotic behavior to turbulent flows—and are designed to assess the models’ ability to capture long-range temporal dependencies. For 1D problems, we use datasets based on the Burgers’ and Kuramoto–Sivashinsky equations, following the setup in Buitrago et al. [3], except that we generate low-resolution datasets by uniformly downsampling the original high-resolution data rather than using cubic interpolation of the trajectory on the finest grid. For 2D problems, we evaluate on the TorusLi dataset introduced by Li et al. [20], which features a fixed forcing and low viscosity regime, as well as the TorusVis and TorusVisForce datasets introduced by Tran et al. [28], which incorporate variable and time-dependent forcing under randomly sampled viscosities in the range  $\nu \in [10^{-5}, 10^{-4}]$ .

**1D Burgers’ Equation.** The Burgers’ equation for scalar velocity field  $u = u(x, t)$  is given by:

$$\partial_t u + u \partial_x u = \nu \partial_{xx} u, \quad (5)$$

where  $\nu > 0$  is the viscosity coefficient, and the equation is considered with periodic boundary conditions. This equation captures the interplay between nonlinear convection and diffusion.

**1D Kuramoto–Sivashinsky Equation.** The Kuramoto–Sivashinsky (KS) equation is a nonlinear PDE known for exhibiting chaotic behavior, and given by:

$$\partial_t u + u \partial_x u + \partial_{xx} u + \nu \partial_{xxxx} u = 0, \quad (6)$$

where  $u = u(x, t)$  is the scalar field of interest, and  $\nu > 0$  is a parameter controlling the system’s diffusivity. The KS equation is studied on a periodic spatial domain.

**2D Navier–Stokes Equations.** The incompressible 2D Navier–Stokes equations describe the motion of fluids. In vorticity form, they describe the evolution of the scalar vorticity  $\omega = \omega(x, y, t)$ :

$$\partial_t \omega + \mathbf{u} \cdot \nabla \omega = \nu \Delta \omega + f, \quad (7)$$

where  $\mathbf{u} = (u, v)$  is the velocity field satisfying  $\nabla \cdot \mathbf{u} = 0$ ,  $\nu > 0$  is the kinematic viscosity, and  $f$  represents external forcing. The velocity field  $\mathbf{u}$  is related to the vorticity through the stream function  $\psi$  as  $\mathbf{u} = \nabla^\perp \psi$ , with  $\Delta \psi = -\omega$ . The equations are considered on a periodic two-dimensional torus.

**Data Preprocessing and Training Setup.** We follow standard practices from prior work [28], including dataset normalization, Gaussian noise augmentation, and teacher forcing. All models use four blocks with consistent hidden dimensions unless otherwise specified. For memory-augmented models, the memory module is placed mid-network, and non-Markovian models use a fixed memory window of  $K = 4$ . We study the effect of teacher forcing on ST-SSM in Appendix C.4 and the effect of varying  $K$  on ST-SSM’s performance in Appendix C.3. Low-resolution datasets are generated by uniform downsampling, and models are trained to minimize the step-wise normalized relative  $\ell_2$  loss. Full details on data generation, preprocessing, and training are provided in Appendices E and F.

## 6 Results

### 6.1 1D Burgers’ Equation

We evaluate model performance on the canonical 1D Burgers’ equation task with  $\nu = 0.001$ , across three temporal resolutions: 128, 64, and 32. As shown in Table 1, ST-SSM achieves state-of-the-art

accuracy at all resolutions, outperforming all baselines by a substantial margin. Compared to recent Fourier-based architectures like FFNO, Multi-Input FFNO, and S4-FFNO, ST-SSM consistently achieves  $2\text{--}3\times$  lower relative  $\mathcal{L}^2$  error across the board. This performance gap becomes even more pronounced at coarser temporal resolutions, underscoring ST-SSM’s ability to model long-range temporal dependencies with stability. While Multi-Input FFNO and S4-FFNO also incorporate memory mechanisms, we observe that restricting the temporal context to a small window ( $\bar{K} = 4$ ) does not significantly degrade ST-SSM’s performance. This suggests that the spatial memory component in our architecture might help compensate for the limited temporal information, enabling the model to maintain strong predictive accuracy under constrained settings.

Beyond accuracy, ST-SSM demonstrates strong parameter efficiency. With just over  $200k$  parameters—nearly an order of magnitude fewer than competing baselines—ST-SSM delivers superior performance across all resolutions. Unlike many Fourier-based models whose parameter counts scale with input resolution and the number of spectral modes used, ST-SSM maintains a constant parameter count, independent of resolution. This fixed cost has the potential to make ST-SSM especially valuable for scientific computing scenarios where memory and compute resources are constrained.

We observe that the relative  $\mathcal{L}^2$  errors reported here are substantially lower than those presented in Buitrago et al. [3], despite using the same benchmark. We suspect this discrepancy stems from differences in normalization strategies which we discuss further detail in Appendix G.

Table 1: Relative  $\mathcal{L}^2$  error on 1D benchmarks at varying resolutions.

Resolution	Architecture	# Parameters	Relative $\mathcal{L}^2$ Error			
			KS			Burgers’
			$\nu = 0.075$	$\nu = 0.1$	$\nu = 0.125$	$\nu = 0.001$
128	U-Net	2,707,905	0.0964	0.0493	0.0120	0.0668
	Factformer (1D)	656,609	0.0522	0.0144	0.0331	0.0152
	FFNO	2,239,618	0.0583	0.0318	0.0227	0.0200
	Multi Input GKT	291,521	0.0710	0.0352	0.0240	0.0356
	Multi Input FFNO	2,239,810	0.0317	0.0172	0.0125	0.0157
	S4-FFNO	2,260,354	0.0320	0.0172	0.0126	0.0159
	ST-SSM (ours)	203,713	<b>0.0086</b>	<b>0.0027</b>	<b>0.0013</b>	<b>0.0070</b>
64	U-Net	2,707,905	0.1535	0.0631	0.0125	0.0580
	Factformer (1D)	656,609	0.0951	0.0168	0.0331	0.0269
	FFNO	1,191,042	0.1185	0.0688	0.0457	0.0225
	Multi Input GKT	160,449	0.1238	0.0495	0.0312	0.0312
	Multi Input FFNO	1,191,234	0.0487	0.0232	0.0168	0.0190
	S4-FFNO	1,211,778	0.0520	0.0247	0.0171	0.0195
	ST-SSM (ours)	203,713	<b>0.0143</b>	<b>0.0048</b>	<b>0.0029</b>	<b>0.0121</b>
32	U-Net	2,707,905	0.1970	0.1243	0.1001	0.0382
	Factformer (1D)	656,609	0.1221	0.0598	0.0274	0.0399
	FFNO	666,754	0.1862	0.1127	0.0986	0.0286
	Multi Input GKT	94,913	0.1258	0.0956	0.0803	0.0384
	Multi Input FFNO	666,946	0.0941	0.0466	0.0320	0.0246
	S4-FFNO	687,490	0.1040	0.0535	0.0379	0.0253
	ST-SSM (ours)	203,713	<b>0.0472</b>	<b>0.0162</b>	<b>0.0088</b>	<b>0.0200</b>

## 6.2 1D Kuramoto–Sivashinsky Equation

We evaluate model performance on the 1D Kuramoto–Sivashinsky (KS) equation across three viscosity regimes ( $\nu = 0.075, 0.1, 0.125$ ) and temporal resolutions of 128, 64, and 32. As shown in Table 1, ST-SSM consistently achieves the lowest relative  $\mathcal{L}^2$  errors in every setting, often by a substantial margin. At resolution 128, for instance, ST-SSM achieves errors of 0.0086, 0.0027, and 0.0013 across the three viscosities, compared to 0.0317–0.0125 for Multi-Input FFNO and 0.0320–0.0126 for S4-FFNO—representing a reduction of over 70% in all cases. This trend persists at lower resolutions, where the performance of all baselines degrades more severely, while ST-SSM remains robust.

In our comparisons between Multi-Input FFNO and S4-FFNO, we observed that when the window size in S4-FFNO was set equal to the number of temporal features being mixed, the two models performed nearly identically across all settings. In contrast, ST-SSM maintains a distinct advantage even under this configuration, suggesting that its spatial-state formulation captures complementary information.

We also encountered frequent instability during training of GKT for some resolutions. This behavior is consistent with previous observations reported in the Buitrago et al. [3], where convergence issues were noted under similar conditions.

Finally, we observed a considerable performance gap between FFNO and its S4-augmented counterparts, particularly pronounced on the KS task. For example, at resolution 64 and  $\nu = 0.1$ , FFNO reaches a relative error of 0.0688, while S4-FFNO and Multi-Input FFNO achieve 0.0247 and 0.0232, respectively—over 60% lower. We attribute this discrepancy in part to the use of direct subsampling in our data preprocessing, which makes the input signal substantially less informative compared to cubic interpolation used in prior work. While FFNO struggles under these conditions, memory-augmented models—and ST-SSM in particular—are able to maintain strong performance, suggesting an advantage in handling degraded temporal information.

Table 2: Relative  $\mathcal{L}^2$  error on 2D Navier–Stokes datasets. All models are evaluated at a spatial resolution of  $64 \times 64$ .

Architecture	# Parameters	Relative $\mathcal{L}^2$ Error		
		TorusLi	TorusVis	TorusVisForce
U-Net	7,763,041	0.0815	0.0751	0.0786
Factformer (2D) [21]	985,697	0.0486	0.0306	0.0345
FFNO	2,239,682	0.0689	0.0340	0.0353
Multi Input GKT	8,418,145	0.1531	0.0882	0.1214
Multi Input FNO2D	67,176,129	0.0477	0.0358	0.0341
S4-FFNO	2,260,418	0.0557	0.0332	0.0341
ST-SSM (ours)	369,665	<b>0.0345</b>	<b>0.0287</b>	<b>0.0286</b>

### 6.3 2D Navier Stokes Equations

**Navier–Stokes with Fixed Viscosity.** We evaluate our model on the TorusLi dataset, which contains vorticity fields generated by solving the 2D incompressible Navier–Stokes equation on the unit torus with a fixed forcing term and low viscosity  $\nu = 10^{-5}$ . This regime is particularly challenging due to reduced diffusion, leading to highly nonlinear and chaotic behavior in the dynamics.

Table 2 reports the relative  $\mathcal{L}^2$  error of various baselines. Among them, full FNO2D achieves an error of 0.0477 with over 67 million parameters. In contrast, our proposed ST-SSM reduces the error to 0.0345—a 27.7% improvement—while using just 369k parameters, a  $182\times$  reduction in model size.

This performance gap is particularly notable given the difference in scaling characteristics. FNO2D leverages a full 2D Fourier transform to model frequency interactions jointly across both spatial dimensions. This leads to a cost that scales as  $\mathcal{O}(N^D)$ , where  $D$  is the number of dimensions and  $N$  is the resolution per dimension—an approach that quickly becomes infeasible for higher-dimensional problems. In contrast, our ST-SSM applies separate 1D operators along each axis in a factorized manner, achieving a more favorable  $\mathcal{O}(N \cdot D)$  complexity while retaining or improving accuracy.

These improvements demonstrate the advantage of temporal memory even in time-invariant contexts, highlighting the role of state-space modeling for better capturing fluid dynamics in low-viscosity regimes. Among several popular variants of such factorized connections we tested, we found our configuration delivered the best performance. For completeness, we report alternative connection strategies in the Appendix D.

**2D Navier-Stokes: Problems with Varying Viscosities and Forces.** We also evaluate our model on the TorusVis and TorusVisForce datasets from the FFNO benchmark [28], where both the viscosity and external forcing vary across trajectories. In TorusVis, the viscosity is sampled uniformly between



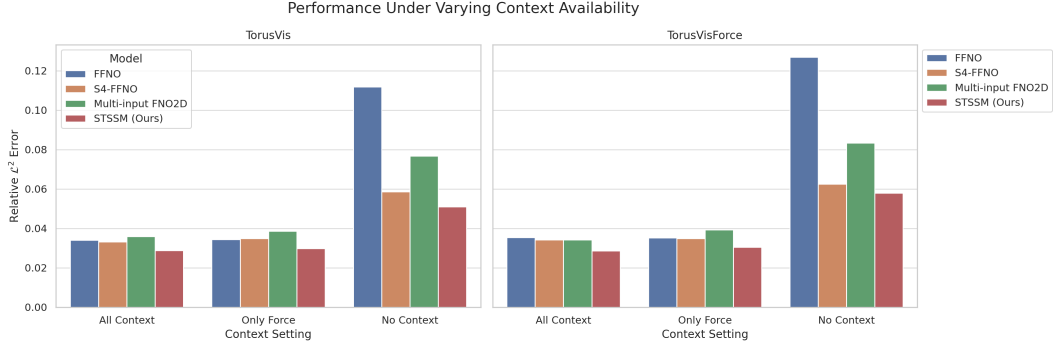


Figure 1: Relative  $\mathcal{L}^2$  error across three levels of contextual information: full context, only forcing, and no context. Lower is better.

$10^{-5}$  and  $10^{-4}$  and the forcing function is time-independent. In contrast, TorusVisForce introduces a time-varying forcing function by setting a phase shift  $\delta = 0.2$ .

Table 2 summarizes the results when full contextual information (i.e., both viscosity and forcing functions) is provided. Our model achieves the lowest errors across both datasets, with improvements over other competitive methods. Our approach shows consistent (slight) advantage.

**Robustness to Missing Contextual Information.** We further investigate the robustness of our model under partial contextual observability, following the experimental protocol of Tran et al. [28]. In this setting, we evaluate models on two ablations: (i) removing the viscosity input, and (ii) removing both viscosity and forcing inputs. These experiments simulate scenarios where key physical parameters are unobserved at test time.

Figure 1 shows the performance degradation under missing context on the TorusVis and TorusVisForce datasets. While all models show increased error as contextual information is removed, our ST-SSM model consistently exhibits smaller performance drops. This demonstrates its ability to infer and internalize contextual dependencies from the temporal evolution of the solution.

These results extend the observations made by Buitrago et al. [3], who showed that temporal memory helps mitigate the effects of resolution loss and noisy data. In our case, we show that memory-based modeling also helps compensate for missing physical parameters—highlighting an additional benefit of incorporating temporal memory into spatiotemporal PDE models.

## 7 Conclusion and Future Work

We have presented the Spatio-Temporal Structured State Space Model (ST-SSM), a compact, adaptive neural operator designed to efficiently learn solution operators for time-dependent partial differential equations. Built on a theoretical understanding of convolutional universality with full receptive field, ST-SSM generalizes and improves upon factorized architectures such as FNO by integrating key adaptive mechanisms—including kernel localization and mode filtering—while enforcing temporal causality. Our spatial-only variant is shown to exactly recover F-FNO, yet ST-SSM dramatically reduces parameter count and computational cost by exploiting a linear  $\mathcal{O}(N \cdot D)$  scaling in contrast to the  $\mathcal{O}(N^D)$  complexity of full high-dimensional convolutions.

Across a suite of 1D and 2D benchmarks, including the Kuramoto–Sivashinsky, Burgers’, and 2D Navier–Stokes equations, ST-SSM consistently achieves lower error and greater efficiency than existing baselines. These gains are especially notable in regimes with limited diffusion or sparse spatial information—where long-term memory and adaptivity are essential. Such results suggest that state-space modeling is not only compatible with operator learning but can provide critical benefits in fluid dynamics and other domains governed by complex temporal-spatial interactions. Beyond outperforming existing methods, our architecture opens the door to tackling higher-dimensional problems that are currently infeasible with full attention or convolutional models, with intended application to astrophysics, cosmology, and space plasma dynamics.

## References

- [1] K. Bhattacharya, B. Hosseini, N. B. Kovachki, and A. M. Stuart. Model reduction and neural networks for parametric pdes. *The SMAI journal of computational mathematics*, 7:121–157, 2021.
- [2] J. Brandstetter, M. Welling, and D. E. Worrall. Lie point symmetry data augmentation for neural pde solvers. In *The International Conference on Machine Learning (ICML)*, 2022.
- [3] R. Buitrago, T. Marwah, A. Gu, and A. Risteski. On the benefits of memory for modeling time-dependent pdes. In *The International Conference on Learning Representations (ICLR)*, 2025.
- [4] S. Cao. Choose a transformer: Fourier or galerkin. In *Advances in neural information processing systems (NeurIPS)*, 2021.
- [5] T. Chen and H. Chen. Universal approximation to nonlinear operators by neural networks with arbitrary activation functions and its application to dynamical systems. *IEEE transactions on neural networks*, 6(4):911–917, 1995.
- [6] C.-W. Cheng, J. Huang, Y. Zhang, G. Yang, C.-B. Schönlieb, and A. I. Aviles-Rivero. Mamba neural operator: Who wins? transformers vs. state-space models for pdes. *arXiv preprint arXiv:2410.02113*, 2024. URL <https://arxiv.org/abs/2410.02113>.
- [7] A. Gu and T. Dao. Mamba: Linear-time sequence modeling with selective state spaces. In *The Conference on Language Modeling (COLM)*, 2024.
- [8] A. Gu, K. Goel, A. Gupta, and C. Ré. On the parameterization and initialization of diagonal state space models. In *Advances in Neural Information Processing Systems (NeurIPS)*, 2022.
- [9] A. Gu, K. Goel, and C. Re. Efficiently modeling long sequences with structured state spaces. In *The International Conference on Learning Representations (ICLR)*, 2022.
- [10] J. K. Gupta and J. Brandstetter. Towards multi-spatiotemporal-scale generalized pde modeling. *Transactions on Machine Learning Research*, 2023.
- [11] D. Hendrycks and K. Gimpel. Gaussian error linear units (gelus). *arXiv preprint arXiv:1606.08415*, 2016. URL <https://arxiv.org/abs/1606.08415>.
- [12] Z. Hu, N. A. Daryakenari, Q. Shen, K. Kawaguchi, and G. E. Karniadakis. State-space models are accurate and efficient neural operators for dynamical systems. *arXiv preprint arXiv:2409.03231*, 2024. URL <https://arxiv.org/abs/2409.03231>.
- [13] N. Kovachki, S. Lanthaler, and S. Mishra. On universal approximation and error bounds for fourier neural operators. *Journal of Machine Learning Research*, 22(290):1–76, 2021. URL <http://jmlr.org/papers/v22/21-0806.html>.
- [14] N. Kovachki, Z. Li, B. Liu, K. Azizzadenesheli, K. Bhattacharya, A. Stuart, and A. Anandkumar. Neural operator: Learning maps between function spaces with applications to pdes. *Journal of Machine Learning Research*, 24(89):1–97, 2023.
- [15] N. B. Kovachki, S. Lanthaler, and A. M. Stuart. Operator learning: Algorithms and analysis. In *Handbook of Numerical Analysis*. Elsevier, 2024. doi: 10.1016/bs.hna.2024.05.009. URL <https://www.sciencedirect.com/science/article/pii/S1570865924000097>.
- [16] S. Lanthaler, S. Mishra, and G. E. Karniadakis. Error estimates for DeepONets: A deep learning framework in infinite dimensions. *Transactions of Mathematics and Its Applications*, 6(1):tnac001, 2022. URL <https://academic.oup.com/imatrm/article-pdf/6/1/tnac001/42785544/tnac001.pdf>.
- [17] S. Lanthaler, Z. Li, and A. M. Stuart. Nonlocality and nonlinearity implies universality in operator learning, 2024. URL <https://arxiv.org/abs/2304.13221>.

- [18] F. Lehmann, F. Gatti, M. Bertin, and D. Clouteau. Seismic hazard analysis with a factorized fourier neural operator (f-FNO) surrogate model enhanced by transfer learning. In *NeurIPS 2023 AI for Science Workshop*, 2023. URL <https://openreview.net/forum?id=xiNRyrBAjt>.
- [19] F. Lehmann, F. Gatti, M. Bertin, and D. Clouteau. 3d elastic wave propagation with a factorized fourier neural operator (f-fno). *Computer Methods in Applied Mechanics and Engineering*, 420:116718, 2024. ISSN 0045-7825. doi: <https://doi.org/10.1016/j.cma.2023.116718>. URL <https://www.sciencedirect.com/science/article/pii/S0045782523008411>.
- [20] Z. Li, N. B. Kovachki, K. Azizzadenesheli, K. Bhattacharya, A. Stuart, A. Anandkumar, et al. Fourier neural operator for parametric partial differential equations. In *The International Conference on Learning Representations (ICLR)*, 2021.
- [21] Z. Li, D. Shu, and A. Barati Farimani. Scalable transformer for pde surrogate modeling. In *Advances in Neural Information Processing Systems (NeurIPS)*, 2023.
- [22] P. Lippe, B. Veeling, P. Perdikaris, R. Turner, and J. Brandstetter. Pde-refiner: Achieving accurate long rollouts with neural pde solvers. In *Advances in Neural Information Processing Systems (NeurIPS)*, 2023.
- [23] L. Lu, P. Jin, G. Pang, Z. Zhang, and G. E. Karniadakis. Learning nonlinear operators via deep-onet based on the universal approximation theorem of operators. *Nature machine intelligence*, 3(3):218–229, 2021.
- [24] H. Mori. Transport, collective motion, and brownian motion. *Progress of theoretical physics*, 33(3):423–455, 1965.
- [25] M. A. Rahman, Z. E. Ross, and K. Azizzadenesheli. U-no: U-shaped neural operators. *Transactions on Machine Learning Research*, 2023.
- [26] B. Raonic, R. Molinaro, T. De Ryck, T. Rohner, F. Bartolucci, R. Alaifari, S. Mishra, and E. de Bézenac. Convolutional neural operators for robust and accurate learning of pdes. In *Advances in Neural Information Processing Systems (NeurIPS)*, 2023.
- [27] M. Takamoto, T. Praditia, R. Leiteritz, D. MacKinlay, F. Alesiani, D. Pflüger, and M. Niepert. Pdebench: An extensive benchmark for scientific machine learning. In *Advances in Neural Information Processing Systems (NeurIPS)*, 2022.
- [28] A. Tran, A. Mathews, L. Xie, and C. S. Ong. Factorized fourier neural operators. In *The International Conference on Learning Representations (ICLR)*, 2023.
- [29] J. Zheng, W. Li, N. Xu, J. Zhu, and X. Zhang. Alias-free mamba neural operator. In *Advances in Neural Information Processing Systems (NeurIPS)*, 2024.
- [30] L. Zhu, B. Liao, Q. Zhang, X. Wang, W. Liu, and X. Wang. Vision mamba: Efficient visual representation learning with bidirectional state space model. In *The International Conference on Machine Learning (ICML)*, 2024.
- [31] R. Zwanzig. Memory effects in irreversible thermodynamics. *Physical Review*, 124(4):983, 1961.

## Appendices

### A Universality of Convolutional NOs

We here provide a rigorous definition of convolutional NOs having a “full field of view”, and provide the precise statement of our sharp universality condition.

#### A.1 Full Field of View

We describe the required full field of view property in greater detail, which we informally stated as a definition before Theorem 4.1 in the main text.

The following assumptions were implicit in that definition: The convolutional NO architecture is of the form

$$\Psi(u) = \mathcal{Q} \circ \mathcal{L}_L \circ \cdots \circ \mathcal{L}_1 \circ \mathcal{R}(u),$$

where the lifting layer  $\mathcal{R}(u)(x) := R(u(x), x)$  and projection layer  $\mathcal{Q}(v(x)) = Q(v(x))$  are given by composition with shallow neural networks  $R, Q$  of width  $H$  (both applied pointwise to the respective input functions). The hidden layers  $\mathcal{L}_\ell$  are given by

$$\mathcal{L}_\ell(v)(x) = \sigma \left( W_\ell v(x) + b_\ell + \int_D \kappa_\ell(x - y; \theta_\ell) v(y) dy \right),$$

with channel width  $H$ . We will assume that  $H$  can be chosen as large as required. For the integral kernel  $\kappa_\ell$ , we assume that, for any choice of  $H$  and matrix  $A_\ell \in \mathbb{R}^{H \times H}$  acting on the channel dimension, there exists a setting of the parameters  $\theta_\ell^*$ , such that  $\kappa_\ell(x; \theta_\ell^*) \in \mathbb{R}^{H \times H}$  is a scalar multiple of  $A$ , i.e. the kernel  $\kappa_\ell(\cdot; \theta_\ell^*)$  is the form

$$\kappa_\ell(x; \theta_\ell^*) \in \mathbb{R}^{H \times H} = g_\ell(x) A_\ell, \quad g_\ell : D \rightarrow \mathbb{R} \text{ some scalar function.} \quad (8)$$

To our knowledge, all proposed architectures, including FNO, factorized FNO, SSM, as well as (UNet-style) convolutional NOs with localized kernels have this property.

The precise definition of the full field of view property is then the following:

**Definition (rigorous).** *An architecture is said to have a full field of view, if for any channel width  $H$  and  $A_\ell \in \mathbb{R}^{H \times H}$  with product  $A_L \cdots A_1 \neq 0$ , we can find parameters such that (8) holds, and the iterated kernel*

$$\bar{\kappa}(x) = (\kappa_L * \cdots * \kappa_1)(x) \equiv (g_L * \cdots * g_1)(x) A_L \cdots A_1,$$

*is nowhere-vanishing, i.e. for any  $x, y \in D$ , we have  $\bar{\kappa}(x - y) \neq 0$ .*

#### A.2 A Sharp Universality Condition

We can now state and prove our universality result for general convolutional NOs.

**Theorem A.1.** *Let  $\mathcal{G} : C(D; \mathbb{R}^{d_i}) \rightarrow C(D; \mathbb{R}^{d_o})$  be a continuous operator, with either  $D \subset \mathbb{R}^d$  compact or  $D = \mathbb{T}^d$  the periodic torus. Let  $\mathcal{K} \subset C(D; \mathbb{R}^{d_i})$  be a compact set of input functions. Let  $\Psi(u)$  be a convolutional NO architecture with a full field of view. Then for any  $\epsilon > 0$ , there exists a channel width  $H$ , and a setting of the weights of  $\Psi$ , such that*

$$\sup_{u \in \mathcal{K}} \sup_{x \in D} |\mathcal{G}(u)(x) - \Psi(u)(x)| \leq \epsilon.$$

*Proof.* For simplicity, we will assume that  $d_i = d_o = 1$ . The proof easily extends to the more general case. The space of continuous operators  $\mathcal{G} : \mathcal{K} \rightarrow C(D)$ ,  $u(x) \mapsto \mathcal{G}(u)(x)$ , is isometrically isomorphic to the space  $C(\mathcal{K} \times D)$ , by identifying  $\mathcal{G}(u, x) := \mathcal{G}(u)(x)$ . By assumption, both  $\mathcal{K}$  and  $D$  are compact sets.

Given the choice of convolutional NO architecture, we now fix  $\kappa_1, \dots, \kappa_L$  such that  $\bar{\kappa}$  is nowhere vanishing. Let us now introduce the set  $\mathbb{A}$  consisting of all operators that can be represented by a choice of channel width  $H$  and a choice of tunable parameters:

$$\mathbb{A} := \left\{ \Psi = \mathcal{Q} \circ \mathcal{L}_L \circ \cdots \circ \mathcal{L}_1 \circ \mathcal{R}, \Psi \text{ is a convolutional NO} \right. \\ \left. \text{with kernels } \kappa_1, \dots, \kappa_L \text{ and channel width } H \right\}.$$

Our goal is to show that  $\mathbb{A} \subset C(\mathcal{K} \times D)$  is dense. We denote by  $\overline{\mathbb{A}}$  the closure of  $\mathbb{A}$  in  $C(\mathcal{K} \times D)$  (set of limit points). To prove that  $\mathbb{A} \subset C(\mathcal{K} \times D)$  is dense, we will use the following result, which follows from the Stone-Weierstrass theorem:

**Lemma A.2.** *A subset  $\mathbb{A} \subset C(\mathcal{K} \times D)$  is dense, if*

- *The constant function  $1 \in \mathbb{A}$ ,*
- *$\mathbb{A}$  separates points: For any  $(u_1, x_1), (u_2, x_2) \in \mathcal{K} \times D$ , there exists  $\Psi \in \mathbb{A}$  such that  $\Psi(u_1, x_1) \neq \Psi(u_2, x_2)$ .*
- *$\mathbb{A}$  is an approximate vector subalgebra:*
  - *$\mathbb{A}$  is closed under addition and scalar multiplication (i.e. vector subspace),*
  - *$\mathbb{A}$  is approximately closed under multiplication: For any  $\Psi_1, \Psi_2$ , the product  $\Psi_1 \cdot \Psi_2 \in \overline{\mathbb{A}}$ , where*

$$(\Psi_1 \cdot \Psi_2)(u, x) = \Psi_1(u, x)\Psi_2(u, x),$$
*is the pointwise multiplication.*

Our goal is to show these properties for  $\mathbb{A}$  to conclude that  $\mathbb{A} \subset C(\mathcal{K} \times D)$  is dense.

**$\mathbb{A}$  contains constants.** It is very easy to show that the constant function  $1 \in \mathbb{A}$ , by defining a convolutional NO that disregards the input and has constant output = 1.

**$\mathbb{A}$  is an approximate subalgebra.** To show the other properties, we first note that  $\mathbb{A}$  is closed under scalar multiplication and under addition, i.e.

$$\Psi_1, \Psi_2 \in \mathbb{A} \Rightarrow \lambda_1 \Psi_1 + \lambda_2 \Psi_2 \in \mathbb{A}, \quad \forall \lambda_1, \lambda_2 \in \mathbb{R}.$$

If  $H_1$  and  $H_2$  are the channel widths of  $\Psi_1$  and  $\Psi_2$ , respectively, this conclusion follows by a simple parallelization of  $\Psi_1$  and  $\Psi_2$ , and employing the last projection  $\mathcal{Q}$ -layer to sum (and scale) the parallelized results. Thus,  $\mathbb{A}$  is a vector subspace of  $C(\mathcal{K} \times D)$ .

To show that  $\mathbb{A}$  is approximately closed under multiplication, i.e.  $\Psi_1, \Psi_2 \in \mathbb{A}$  implies that  $\Psi_1 \cdot \Psi_2 \in \overline{\mathbb{A}}$ , we fix arbitrary  $\Psi_1, \Psi_2 \in \mathbb{A}$ . We will denote by  $\hat{\Psi}_j$  the NO  $\Psi_j$  for  $j = 1, 2$ , but where the last  $\mathcal{Q}$  projection-layer has been removed:

$$\Psi_1 \equiv \mathcal{Q}_1 \circ \hat{\Psi}_1, \quad \Psi_2 \equiv \mathcal{Q}_2 \circ \hat{\Psi}_2.$$

Assuming wlog that the channel width  $H_1 = H_2 = H$  (otherwise, we can pad the channel width by zeros), we note that these incomplete NOs  $\hat{\Psi}_1$  and  $\hat{\Psi}_2$  define continuous mappings  $\mathcal{K} \times D \rightarrow \mathbb{R}^H$ . Since  $\mathcal{K} \times D$  is compact, it follows that also the images  $\hat{\Psi}_j(\mathcal{K} \times D) \subset \mathbb{R}^H$  are compact (since compact sets are mapped to compact sets under continuous maps). In particular, there exists  $B > 0$ , such that

$$\hat{\Psi}_1(u, x), \hat{\Psi}_2(u, x) \in [-B, B]^H, \quad \forall u \in \mathcal{K}, x \in D.$$

Consider now  $\mathcal{Q}_1$  and  $\mathcal{Q}_2$ , i.e. the last layers of  $\Psi_1$  and  $\Psi_2$ , respectively. The following product mapping

$$[-B, B]^H \times [-B, B]^H \rightarrow \mathbb{R}, \quad (v_1, v_2) \rightarrow \mathcal{Q}_1(v_1) \cdot \mathcal{Q}_2(v_2),$$

is continuous. By the universality of shallow neural networks, for any  $\epsilon > 0$ , there thus exists a shallow net  $\mathcal{Q} : \mathbb{R}^{2H} \rightarrow \mathbb{R}$ , such that

$$\sup_{|v_1|_\infty, |v_2|_\infty \leq B} |\mathcal{Q}(v_1, v_2) - \mathcal{Q}_1(v_1) \cdot \mathcal{Q}_2(v_2)| \leq \epsilon.$$

Define now a new NO as  $\Psi(u, x) := \mathcal{Q}([\hat{\Psi}_1(u, x), \hat{\Psi}_2(u, x)])$ , i.e.  $\mathcal{Q}$  applied to the parallelization of  $\hat{\Psi}_1$  and  $\hat{\Psi}_2$ . Then

$$\begin{aligned} & \sup_{\mathcal{K} \times D} |\Psi(u, x) - \Psi_1(u, x) \cdot \Psi_2(u, x)| \\ &= \sup_{\mathcal{K} \times D} |\mathcal{Q}([\hat{\Psi}_1(u, x), \hat{\Psi}_2(u, x)]) - \mathcal{Q}_1(\hat{\Psi}_1(u, x)) \cdot \mathcal{Q}_2(\hat{\Psi}_2(u, x))| \\ &\leq \sup_{|v_1|_\infty, |v_2|_\infty \leq B} |\mathcal{Q}(v_1, v_2) - \mathcal{Q}_1(v_1) \cdot \mathcal{Q}_2(v_2)| \\ &\leq \epsilon. \end{aligned}$$

Since  $\epsilon > 0$  was arbitrary, this shows that  $\Psi_1 \cdot \Psi_2$  is a limit point of  $\Psi \in \mathbb{A}$ , thus  $\Psi_1 \cdot \Psi_2 \in \overline{\mathbb{A}}$ . We conclude from the above that  $\mathbb{A}$  is an approximate vector subalgebra.

**$\mathbb{A}$  separates points.** To conclude our proof, it only remains to show that  $\mathbb{A}$  separates points. Let  $(u_1, x_1) \neq (u_2, x_2)$  be two distinct elements in  $\mathcal{K} \times D$ . There are two cases: Either  $x_1 \neq x_2$ , or  $x_1 = x_2$  and  $u_1 \neq u_2$ .

**Case 1:**  $x_1 \neq x_2$ . We want to construct  $\Psi \in \mathbb{A}$ , such that  $\Psi(u_1, x_1) \neq \Psi(u_2, x_2)$ . This is easy, since we can always use the lifting layer  $\mathcal{R}$  to eliminate the dependency of  $\Psi$  on the  $u$ -variable. Once the weights acting on the  $u$ -variable have been set to zero, we then have that  $\Psi(u, x) = \psi(x)$  is an ordinary multilayer perceptron. Since  $x_1 \neq x_2$ , we can easily choose  $\psi$  such that e.g.  $\psi(x_1) = 0$  and  $\psi(x_2) = 1$ . Thus  $\Psi(u_1, x_1) = \psi(x_1) \neq \psi(x_2) = \Psi(u_2, x_2)$ .

**Case 2:**  $x_1 = x_2 = x$  and  $u_1 \neq u_2$ . This is the more difficult case. In the following argument, we will appeal to the universality of shallow neural networks, and their compositions, multiple times. We will forego the tedious  $\epsilon$ - $\delta$  estimates, and instead sketch out the general idea; filling in the details is a straight-forward (and boring...), exercise that would not provide any additional insight.

We construct  $\Psi$  as follows: First, given matrices  $A_\ell$  and functions  $g_\ell$  as in the (rigorous) definition of “full field of view”, we choose the weights of the hidden layers  $\mathcal{L}_\ell$ , such that

$$\mathcal{L}_\ell(v)(x) = \sigma \left( A_\ell \int_D g_\ell(x - y) v(y) dy + b_\ell \right).$$

This is possible by assumption on the convolutional NO architecture, cp. (8). By universality of shallow neural networks, we can choose  $H$  sufficiently large, and choose matrices  $C_*$ ,  $A_*$  and biases  $\alpha_*$ ,  $\beta_*$ , such that for all relevant input vectors  $\xi = (\xi_1, 0, \dots, 0)$  (effectively one-dimensional), we have

$$C_* \sigma(A_* \xi + \beta_*) + \alpha_* \approx \xi, \quad (9)$$

i.e. the resulting shallow neural network is an approximation of the identity on one-dimensional  $\xi$ , to any desired accuracy.

We now momentarily focus on the case  $L = 2$ . In this case, we choose  $A_1 = A_*$ ,  $b_1 = b_*$ , then choose  $A_2 = A_* C_*$ , and bias  $b_2 = \alpha_* \int_D g(x - y) dy + \beta_*$ , so that

$$\mathcal{L}_2 \circ \mathcal{L}_1(v)(x) = \sigma \left( A_2 \int_D g_2(x - y) \mathcal{L}_1(v)(y) dy + b_2 \right),$$

where

$$A_2 \int_D g_2(x - y) \mathcal{L}_1(v)(y) dy + b_2 = A_* \int_D g_2(x - y) \{C_* \mathcal{L}_1(v)(y) + \alpha_*\} dy + b_*.$$

We now note that, by construction, we have for any hidden state function of the form  $v(y) = [v_1(y), 0, \dots, 0]^T$ :

$$C_* \mathcal{L}_1(v)(y) + \alpha_* = C_* \sigma(A_*(g_1 * v)(y) + \beta_*) + \alpha_* \approx \int_D g_1(y - z) v(z) dz,$$

where we have used (9) and note that this approximation is to any desired accuracy. It follows that also

$$\begin{aligned} \mathcal{L}_2 \circ \mathcal{L}_1(v)(x) &\approx \sigma \left( A_* \int_D g_2(x - y) \int_D g_1(y - z) v(z) dz dy + b_* \right) \\ &= \sigma \left( A_* \int_D (g_2 * g_1)(x - y) v(y) dy + b_* \right), \end{aligned}$$

to any desired accuracy. This shows that for two hidden layers  $\mathcal{L}_1, \mathcal{L}_2$  there exists a choice of the parameters, such that for a hidden state  $v(x) = (v_1(x), 0, \dots, 0)$ , we can obtain an arbitrarily good approximation

$$\mathcal{L}_2 \circ \mathcal{L}_1(v)(x) \approx \sigma \left( A_* \int_D (g_2 * g_1)(x - y) v(y) dy + b_* \right).$$

Iterating this argument, for general  $L \geq 2$ , we start from  $\mathcal{L}_L \circ \mathcal{L}_{L-1} \circ \dots \mathcal{L}_1$ , and we first choose the weights of  $\mathcal{L}_L$  and  $\mathcal{L}_{L-1}$  such that

$$\mathcal{L}_L \circ \mathcal{L}_{L-1}(v)(x) \approx \sigma \left( A_* \int_D (g_L * g_{L-1})(x-y)v(y) dy + b_* \right).$$

This can be done by the argument employed for the case  $L = 2$ . Next, we can apply the same argument again to choose the weights of  $\mathcal{L}_{L-2}$ , such that

$$\begin{aligned} \mathcal{L}_L \circ \mathcal{L}_{L-1} \circ \mathcal{L}_{L-2}(v)(x) &= (\mathcal{L}_L \circ \mathcal{L}_{L-1}) \circ \mathcal{L}_{L-2}(v)(x) \\ &\approx \sigma \left( A_* \int_D (g_L * g_{L-1} * g_{L-2})(x-y)v(y) dy + b_* \right), \end{aligned}$$

and continue similarly, until

$$\mathcal{L}_L \circ \dots \circ \mathcal{L}_1(v)(x) \approx \sigma \left( A_* \int_D (g_L * \dots * g_1)(x-y)v(y) dy + b_* \right),$$

to any desired accuracy. This argument is based on the assumption that  $v(x) = (v_1(x), 0, \dots, 0)$ .

We next add a projection layer  $\mathcal{Q}$  to this composition, of the form  $\mathcal{Q}(v)(x) = Q(C_*v(x) + \alpha_*)$ , where  $\mathcal{Q}$  is a shallow neural network, to obtain

$$\mathcal{Q} \circ \mathcal{L}_L \circ \dots \circ \mathcal{L}_1(v)(x) \approx Q \left( \int_D \bar{g}(x-y)v(y) dy \right), \quad \bar{g}(x) := (g_L * \dots * g_1)(x).$$

Recall that  $\bar{g}(x-y) \neq 0$  for all  $x, y \in D$ , by assumption (full field of view).

Pre-composing with a lifting layer  $\mathcal{R}(u)(x) = R(u(x), x)$ , which we choose to have only a non-vanishing first component on the output-side, i.e.  $R(u(x), x) = (R_1(u(x), x), 0, \dots, 0)$ , it follows that we can construct  $\Psi(u)(x) := \mathcal{Q} \circ \mathcal{L}_L \circ \dots \circ \mathcal{L}_1 \circ \mathcal{R}$ , such that

$$\Psi(u)(x) \approx Q \left( \int_D \bar{g}(x-y)R_1(u(y), y) dy \right),$$

where the approximation error can be made arbitrarily small. Here, we are still free to choose  $Q$  and  $R_1$ . Our goal is to choose them in such a way that for our given functions  $u_1 \neq u_2$  and the given point  $x \in D$ , we have  $\Psi(u_1)(x) \neq \Psi(u_2)(x)$ . We will choose  $Q$  as an approximation of the identity on the first component, so that

$$\Psi(u)(x) \approx \int_D \bar{g}(x-y)R_1(u(y), y) dy.$$

By assumption,  $\bar{g}(x-y) \neq 0$  is non-vanishing for all  $y \in D$ . Since  $u_1 \neq u_2$ , there exists  $y_0 \in D$  such that  $u_1(y_0) \neq u_2(y_0)$ . We may wlog assume that  $u_1(y_0) < \tau_1 < \tau_2 < u_2(y_0)$  for some  $\tau_1, \tau_2 \in \mathbb{R}$ . By continuity of  $u_1, u_2$ , there exists  $\delta > 0$ , such that  $\max_{B_\delta(y_0)} u_1(y) < \tau_1 < \tau_2 < \min_{B_\delta(y_0)} u_2(y)$ . By the universality of the shallow network  $R_1$ , we can choose  $R_1$ , such that we approximately have

$$R_1(\eta, y) \approx \rho_\delta(y - y_0)h_{\tau_1, \tau_2}(\eta),$$

where  $\rho_\delta(\cdot - y_0)$  is a non-negative function supported inside  $B_\delta(y_0)$ , and  $h_{\tau_1, \tau_2}(\cdot)$  is a non-negative function, such that

$$h_{\tau_1, \tau_2}(\eta) = \begin{cases} 1, & (\eta > \tau_2), \\ 0, & (\eta < \tau_1). \end{cases}$$

Since  $\bar{g}(x-y)$  is non-vanishing for all  $x, y \in D$ , we can further refine our choice of  $\rho_\delta$ , to ensure that

$$\int_D \bar{g}(x-y)\rho_\delta(y - y_0) dy \neq 0.$$

It then follows that

$$R_1(u_1(y), y) \approx \rho_\delta(y - y_0)h_{\tau_1, \tau_2}(u_1(y)) \equiv 0,$$

and

$$R_1(u_2(y), y) \approx \rho_\delta(y - y_0)h_{\tau_1, \tau_2}(u_2(y)) \equiv \rho_\delta(y - y_0).$$

In particular, we conclude that – to any desired accuracy – we can construct  $\Psi(u)$ , such that

$$\Psi(u_1)(x) \approx \int_D \bar{g}(x-y) R_1(u_1(y), y) dy \approx 0$$

and

$$\Psi(u_2)(x) \approx \int_D \bar{g}(x-y) R_1(u_2(y), y) dy \approx \int_D \bar{g}(x-y) \rho_\delta(y-y_0) dy \neq 0.$$

In particular, upon making the approximation errors sufficiently small, it follows that there exists  $\Psi \in \mathbb{A}$  such that  $\Psi(u_1)(x) \neq \Psi(u_2)(x)$ . This finally shows that  $\mathbb{A}$  separates points.

Our proof of the universality of  $\mathbb{A} \subset C(\mathcal{K} \times D)$  now concludes by application of the Stone-Weierstrass theorem (cp. Lemma A.2).

□

## B Architecture Diagrams

The following diagrams illustrate the ST-SSM architecture.

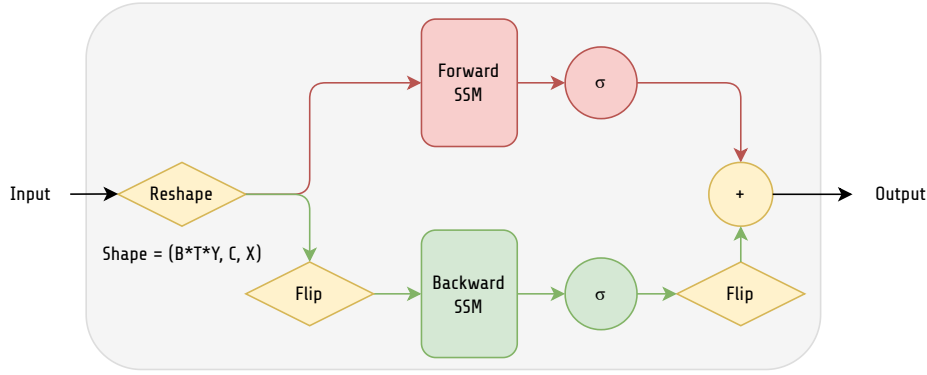


Figure 2: Detailed illustration of the spatial bidirectional SSM module. The input is processed through both a forward spatial SSM and a flipped backward spatial SSM. Each path includes a residual connection and nonlinear activation, and their outputs are aggregated to form the final output.

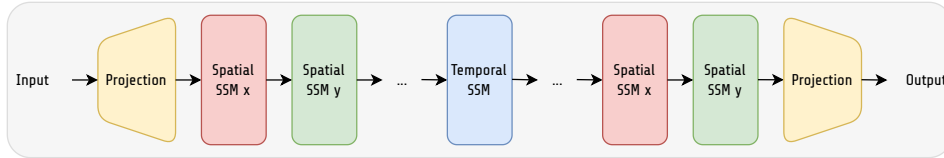


Figure 3: Overview of the full model architecture, which combines 1D Markovian spatial SSM modules with a non-Markovian temporal SSM to model spatiotemporal dynamics. The spatial SSMs are applied sequentially across spatial dimensions, while temporal dependencies are captured by aggregating hidden states across time. The location of the temporal SSM within the model stack is a tunable hyperparameter, allowing flexibility based on the characteristics of the target PDE.

## C Ablation Studies

### C.1 Unidirectional Spatial SSM

We conduct an ablation study to evaluate the importance of the bidirectional spatial module in our ST-SSM architecture on 1D Burgers' Equation. To ensure a fair comparison that isolates the effect of



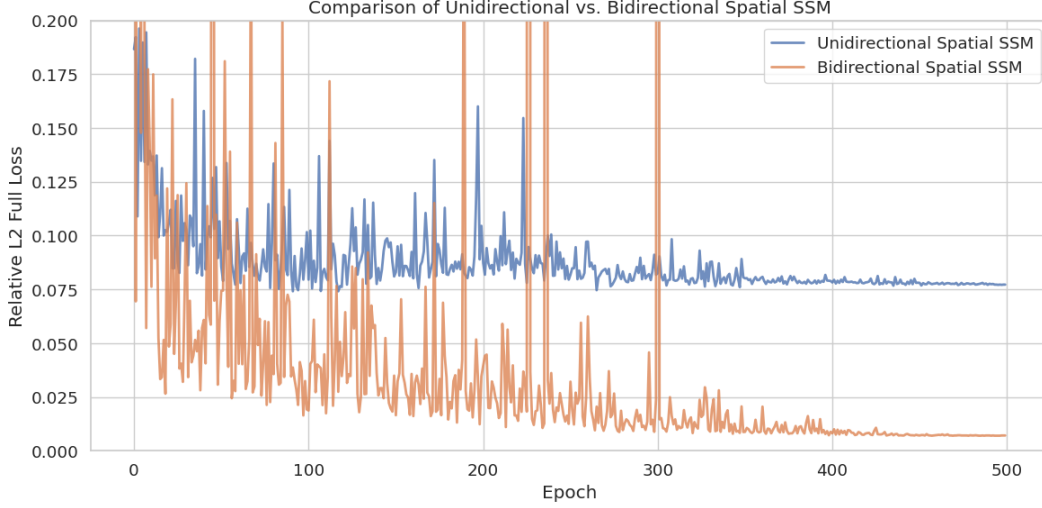


Figure 4: Training curves comparing the unidirectional and bidirectional spatial SSMs on the TorusLi dataset. The unidirectional variant plateaus early, failing to capture global spatial dependencies.

directionality, we construct a unidirectional model with the same parameter count as the full ST-SSM. This is done by stacking 8 layers of forward-only spatial SSM blocks and inserting a single temporal SSM layer in the middle.

As shown in Figure 4, the unidirectional variant fails to capture the dynamics effectively. Its training curve plateaus early, and the relative  $\mathcal{L}^2$  error stagnates around 0.075. In contrast, the full bidirectional model continues to improve and ultimately reaches a much lower error of approximately 0.007—more than ten times better. These results highlight that unidirectional spatial SSMs are fundamentally limited in their representational capacity for 2D PDEs and act as non-universal approximators in this setting – indeed, this unidirectional spatial SSM *is lacking* a full field of view, violating the criterion for universality in Theorem 4.1. Bidirectional context is essential to capture the long-range spatial dependencies needed for accurate forecasting.

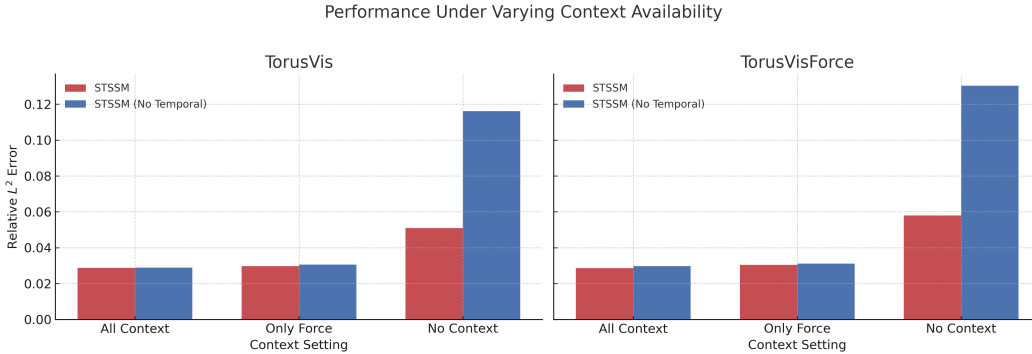


Figure 5: Performance under varying context availability, comparing the full ST-SSM with its variant without the temporal module on TorusVis and TorusVisForce datasets.

## C.2 Effect of Removing the Temporal SSM Component

To isolate the contribution of the temporal module in our ST-SSM architecture, we repeat the "Robustness to Missing Contextual Information" experiment conducted in Section 6.3, but this time with an ablated version of our model that removes the temporal state-space model (SSM) component while keeping all other settings identical. This variant retains the same spatial processing architecture but lacks the capacity to explicitly model temporal dependencies.

Figure 5 reports the relative  $\mathcal{L}^2$  error for both variants on the TorusVis and TorusVisForce datasets. Adding the temporal SSM component does not lead to degraded performance, in contrast to prior work suggesting that Markovian assumptions often result in better model behavior [28, 22]. Across all context configurations, the performance gap between the full and ablated variants remains negligible, confirming that incorporating temporal modeling does not hinder predictive accuracy.

More importantly, in the most challenging *No Context* setting—where both forcing and viscosity information are missing—the full ST-SSM shows a clear advantage over its ablated counterpart. This indicates that the temporal SSM, even when operating over a short memory window ( $K = 4$ ), effectively captures temporal dependencies that help compensate for the absence of contextual inputs, thereby enhancing robustness to missing information.

### C.3 Effect of Varying the Memory Window Size

We investigate how the choice of memory window size  $K$  affects the performance of our ST-SSM model on the KS dataset with  $\nu = 0.075$ . This hyperparameter controls how many past spatial feature maps are accessible to the model during temporal state updates. All results reported in this section are obtained from models trained *without teacher forcing* to better reflect deployment conditions.

As shown in Figure 6, increasing  $K$  consistently improves performance up to around  $K = 8$ . Beyond this point, the performance gains become increasingly marginal, and the validation loss begins to plateau. Notably, setting  $K = 0$ , which corresponds to no temporal memory, results in significantly degraded performance. These results highlight the critical importance of temporal memory in modeling complex spatiotemporal dynamics, while also suggesting diminishing returns beyond a moderate window size.

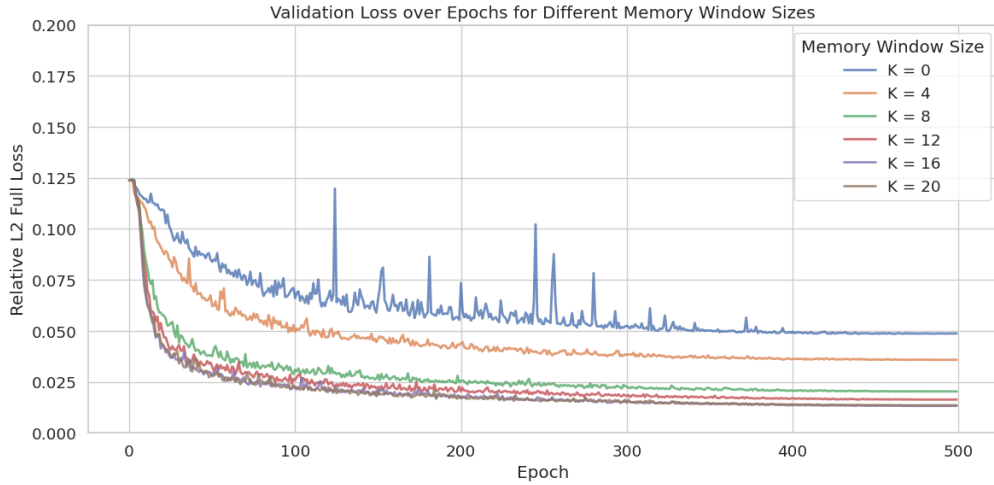


Figure 6: Validation  $\mathcal{L}^2$  loss over training epochs for different memory window sizes  $K$  on the KS dataset ( $\nu = 0.075$ ). Increasing the window improves performance until around  $K = 8$ , after which gains diminish.

### C.4 Effect of Teacher Forcing on ST-SSM Performance

**Case Study: 1D KS with  $\nu = 0.075$  at Low Resolution.** While prior work such as FFNO [28] suggests that teacher forcing can improve model performance by stabilizing training, we observe a different trend for our ST-SSM architecture, particularly in low-resolution regimes. To investigate this, we revisit the 1D Kuramoto–Sivashinsky (KS) dataset with  $\nu = 0.075$ , where reduced spatial resolution poses a significant challenge.

We train ST-SSM with teacher forcing across various memory window sizes ( $K = 0$  to 20), and present the results in Figure 7. Compared to the non-teacher-forced variant (Figure 6), training with teacher forcing leads to noticeably less stable optimization, slower convergence, and consistently higher final relative  $\mathcal{L}^2$  errors. Moreover, while performance still improves with longer memory, the

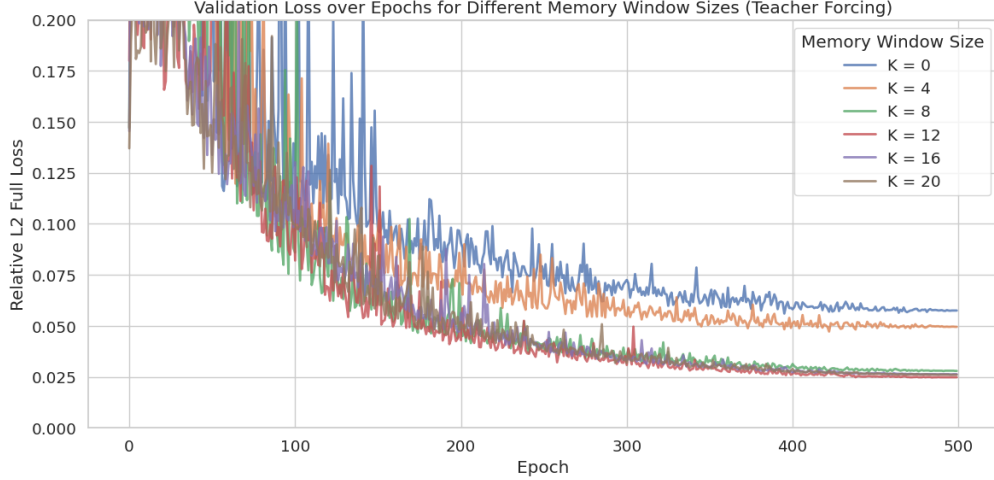


Figure 7: Validation  $\mathcal{L}^2$  loss over training epochs on the KS dataset ( $\nu = 0.075$ ) using teacher forcing for various memory window sizes  $K$ . Compared to Figure 6, training is less stable and results in higher loss.

gains plateau earlier, and the benefits beyond  $K = 8$  diminish more rapidly than in the non-teacher-forced case.

These findings suggest that in this setting, ST-SSM benefits more from fully autoregressive training, likely due to its strong inductive bias for modeling long-term temporal dependencies without relying on ground-truth guidance.

**General Trends Across 1D and 2D Benchmarks.** To better understand the broader impact of teacher forcing, we compare ST-SSM models trained with and without teacher forcing across all 1D and 2D benchmarks (Tables 3 and 4).

In 1D settings, results are mixed: at higher resolutions (e.g., 128), teacher forcing slightly improves performance in some cases (e.g., KS with  $\nu = 0.1$  and  $\nu = 0.125$ ), but at lower resolutions, non-teacher-forced models generally perform better—especially in the challenging  $\nu = 0.075$  KS setup. These results suggest that autoregressive training may confer more robustness in low-resolution or harder regimes, where model predictions diverge more easily from ground truth.

In contrast, across all 2D Navier–Stokes benchmarks, teacher forcing consistently yields better performance. This suggests that for higher-dimensional systems with complex spatiotemporal interactions, teacher forcing can help stabilize training and guide the model toward more accurate trajectories.

Overall, while the effect of teacher forcing appears to be dataset- and resolution-dependent, we find that non-teacher-forced training can be highly effective in 1D regimes, particularly under low resolution. In contrast, for complex 2D flows, teacher forcing remains a valuable tool for improving predictive accuracy.

## D Comparison of Factorized Architectural Variants

In this section, we explore how different architectural factorization strategies affect performance on the TorusLi dataset. Specifically, we examine two popular alternatives to our default ST-SSM spatial block.

**ST-SSM-VM (Vision Mamba style).** This variant adapts the Vision Mamba architecture by replacing the Mamba core with our spatial SSM block. The key idea is to preserve Vision Mamba’s flattened zigzag scanning structure in 2D, allowing bidirectional processing over a 1D sequence obtained from flattening the spatial grid. After bidirectional processing over the first spatial axis, the result is passed through a mixing linear projection before a second pass along the alternate axis, again

Table 3: Relative  $\mathcal{L}^2$  error on 1D benchmarks at varying resolutions.

Resolution	Architecture	Relative $\mathcal{L}^2$ Error			
		KS			Burgers'
		$\nu = 0.075$	$\nu = 0.1$	$\nu = 0.125$	$\nu = 0.001$
128	ST-SSM (Teacher Forcing)	0.0086	<b>0.0027</b>	<b>0.0013</b>	<b>0.0070</b>
	ST-SSM (No Teacher Forcing)	<b>0.0076</b>	0.0034	0.0019	<b>0.0070</b>
64	ST-SSM (Teacher Forcing)	0.0143	0.0048	0.0029	0.0121
	ST-SSM (No Teacher Forcing)	<b>0.0135</b>	<b>0.0042</b>	<b>0.0023</b>	<b>0.0114</b>
32	ST-SSM (Teacher Forcing)	0.0472	0.0162	0.0088	0.0200
	ST-SSM (No Teacher Forcing)	<b>0.0358</b>	<b>0.0135</b>	<b>0.0071</b>	<b>0.0171</b>

Table 4: Relative  $\mathcal{L}^2$  error on 2D Navier–Stokes datasets. All models are evaluated at a spatial resolution of  $64 \times 64$ .

Architecture	Relative $\mathcal{L}^2$ Error		
	TorusLi	TorusVis	TorusVisForce
ST-SSM (Teacher Forcing)	<b>0.0345</b>	<b>0.0287</b>	<b>0.0286</b>
ST-SSM (No Teacher Forcing)	0.0546	0.0385	0.0371

using bidirectional spatial SSMs and linear mixing. This model maintains Vision Mamba’s emphasis on alternating directional fusion while leveraging the structure of our SSM.

**ST-SSM-FF (FFNO style).** In this variant, we discard the original spatial block of ST-SSM and instead adopt the FFNO-style connection, where spatial context is aggregated through two 1D sweeps: one across the  $x$ -axis and one across the  $y$ -axis. Each sweep involves a forward and backward spatial SSM applied independently along that axis, and the outputs from both axes are summed together. This approach highlights the role of directional decoupling in factorized Fourier models and contrasts with the fused zigzag sweep in ST-SSM-VM.

Pseudocode for both ST-SSM-FF and ST-SSM-VM variants is provided in Figure 8.

**FNO2D-R (Reduced Fourier Kernel).** To verify that the gains of ST-SSM are not trivially due to kernel simplification, we construct a reduced FNO2D model, denoted as FNO2D-R. In this variant, we remove the output channel mixing in the Fourier kernel by modifying the kernel from:

```
self.weights = nn.Parameter(self.scale * torch.rand(
    in_channels, out_channels, modes1, modes2, dtype=torch.cfloat))
...
return torch.einsum("bixy,ioxy->boxy", input, weights)
```

to:

```
self.weights = nn.Parameter(self.scale * torch.rand(
    in_channels, modes1, modes2, dtype=torch.cfloat))
...
return input * weights
```

This isolates the contribution of full channel-wise Fourier mixing and allows for a more controlled comparison against ST-SSM.

As shown in Table 5, our original ST-SSM achieves the best performance among all tested variants, demonstrating that both our architectural choices and structured state-space modeling contribute meaningfully to the observed improvements.

```

# ST-SSM-VM (Vision Mamba Style)
x_flat = flatten_spatial(x)

# First zigzag sweep
x_fwd = SSM_flat_forward(x_flat)
x_bwd = SSM_flat_backward(reverse(
    x_flat))
z1 = permute_channels(x_fwd + x_bwd
)
x = linearT(z1) + x_flat

# Second zigzag sweep
x_fwd2 = SSM_flat_forward(x)
x_bwd2 = SSM_flat_backward(reverse(
    x))
z2 = permute_channels(x_fwd2 +
    x_bwd2)
x = linearT2(z2) + x

x_out = reshape_spatial(x)

```

Listing 1: ST-SSM-VM (Vision Mamba style)

```

# ST-SSM-FF (FFNO-style)
residual = x

# X-axis sweep
x1 = reshape_for_x_sweep(x)
x1_fwd = SSM_x_forward(x1)
x1_bwd = reverse(SSM_x_backward(
    reverse(x1)))
x1_combined = reshape_back(x1_fwd +
    x1_bwd)

# Y-axis sweep
y1 = reshape_for_y_sweep(x)
y1_fwd = SSM_y_forward(y1)
y1_bwd = reverse(SSM_y_backward(
    reverse(y1)))
y1_combined = reshape_back(y1_fwd +
    y1_bwd)

# Combine and project
z = x1_combined + y1_combined
z = backcast_ff(z)
output = z + residual

```

Listing 2: ST-SSM-FF (FFNO-style connection)

Figure 8: Pseudocode for two spatial architectural variants of ST-SSM: Vision Mamba-style (left) and FFNO-style (right).

Table 5: Relative  $\mathcal{L}^2$  error on the TorusLi dataset for different factorized architectural variants. All models are evaluated at a spatial resolution of  $64 \times 64$ .

Architecture	# Parameters	Relative $\mathcal{L}^2$ Error
		TorusLi
ST-SSM-VM	402,945	0.0495
ST-SSM-FF	503,297	0.0403
FNO2D-R	1,115,841	0.0718
ST-SSM (ours)	369,665	<b>0.0345</b>

## E Data Preprocessing and Training Details

### E.1 Training Objective.

We train the model by minimizing the empirical risk over the dataset of trajectories. Given a loss function  $\ell : L^2(\Omega; \mathbb{R}^V) \times L^2(\Omega; \mathbb{R}^V) \rightarrow \mathbb{R}$ , we solve:

$$\theta^* = \arg \min_{\theta} \frac{1}{N} \sum_{i=1}^N \frac{1}{N_{\text{out}}} \sum_{t \in \mathcal{T}_{\text{out}}} \ell \left( u^{(i)}(t, x), \Psi_{\theta, t} \left( u^{(i)}(t', x) |_{t' \in \mathcal{T}_{\text{in}}} \right) \right), \quad (10)$$

where  $\Psi_{\theta, t}(\cdot)$  denotes the prediction at time  $t \in \mathcal{T}_{\text{out}}$ . As our loss  $\ell$ , we employ relative  $\mathcal{L}^2$ -error, discussed below. The formulation (10) enables the model to learn the entire future evolution of the system dynamics from a finite observed window, rather than stepwise or autoregressive forecasting.

### E.2 Evaluation Metric.

Performance is reported wrt. the following relative  $\mathcal{L}^2$  error:

$$\text{Relative } \mathcal{L}^2(u(t, x), \hat{u}(t, x)) = \frac{\|u(t, x) - \hat{u}(t, x)\|_2}{\|u(t, x)\|_2}, \quad (11)$$

where  $\|\cdot\|_2$  denotes the squared norm over all spatial locations and time steps in the output horizon.

### E.3 Data Preprocessing and Training Setup

We normalize all input data to the range  $[0, 1]$  (see Appendix G for further discussion), and add Gaussian noise with a standard deviation randomly sampled between  $[0.001, 0.01]$  to increase robustness. All models, except the Galerkin Transformer (GKT), are trained for 500 epochs using the AdamW optimizer with an initial learning rate of  $10^{-3}$ , weight decay of  $10^{-4}$ , and a cosine annealing learning rate schedule. We employ teacher forcing during training unless otherwise noted.

To simulate low-resolution scenarios, we generate downsampled versions of the original datasets by uniformly subsampling in time. All models are trained to minimize the normalized step-wise relative  $\ell_2$  loss, and evaluation is reported using the full-sequence relative  $\ell_2$  error.

### E.4 Baseline Model Architectures

Unless otherwise specified, all models use four blocks with a channel width of 64. Intermediate and output linear layers have a hidden size of 128 (i.e., twice the channel width). **With the exception of FFNO, multi-input FNO, and our ST-SSM on 1D problems, we adopt the “optimal” hyperparameter settings (i.e., number of layers, hidden dimension, and expansion size of linear layers) reported by Buitrago et al. [3].** The U-Net we use is even larger, containing more parameters than this standard baseline. For memory-augmented architectures, the memory module is inserted after the first two blocks and before the last two. For all non-Markovian models, we fix the memory window size to  $K = 4$  across experiments; the impact of varying  $K$  on ST-SSM is explored in Appendix C.3.

We adopt a simple spatial positional encoding scheme shared across all models. In 1D, for a grid with  $f$  equispaced points over the interval  $[0, L]$ , the positional encoding  $E \in \mathbb{R}^f$  is defined as  $E_i = \frac{i}{L}$  for  $0 \leq i < f$ . In 2D, for a  $f \times f$  grid over  $[0, L_x] \times [0, L_y]$ , the encoding is  $E_{ij} = (\frac{i}{L_x}, \frac{j}{L_y})$ . The input lifting operator  $r_{\text{in}}$  is a shared linear layer that maps the concatenation of input features and positional encoding from  $\mathbb{R}^{2+k}$ , where  $k$  is the number of features, to the hidden space  $\mathbb{R}^h$ , applied pointwise across the spatial grid. Similarly, a shared decoder  $r_{\text{out}}$  maps from  $\mathbb{R}^h$  back to  $\mathbb{R}$ . For all models containing an FNO or FFNO module, we follow the setup in Buitrago et al. [3] and retain all available Fourier modes by setting  $k_{\text{max}} = \lfloor \frac{f}{2} \rfloor$ , where  $f$  denotes the spatial resolution.

**Factorized Fourier Neural Operator (FFNO).** The Factorized Fourier Neural Operator (FFNO), introduced by Tran et al. [28], extends the original Fourier Neural Operator (FNO) [20] by modifying how the spectral integral kernel is applied. Each FFNO layer operates on a spatial grid of size  $|S|$  and a hidden dimension  $h$ , and is defined as a residual block:

$$\ell(v) = v + \text{Linear}_{h \rightarrow h'} \circ \sigma \circ \text{Linear}_{h' \rightarrow h} \circ \mathcal{K}(v),$$

where  $\sigma$  denotes the GeLU activation function [11], and  $h'$  is an intermediate dimensionality used within the nonlinear mapping. The integral operator  $\mathcal{K}$  transforms  $v$  in the Fourier domain and is computed by aggregating across spatial dimensions:

$$\mathcal{K}(v) = \sum_{\alpha=1}^d \text{IFFT}_{\alpha} [R_{\alpha} \cdot \text{FFT}_{\alpha}(v)],$$

where  $\text{FFT}_{\alpha}$  and  $\text{IFFT}_{\alpha}$  are the (inverse) discrete Fourier transforms applied along the  $\alpha$ -th spatial axis, and  $R_{\alpha} \in \mathbb{C}^{h^2 \times k_{\text{max}}}$  are learned complex-valued projection matrices for each dimension.

**Multi Input (Factorized) Fourier Neural Operator (Multi Input FNO/FFNO).** For 2D problems we use a modified version of the original Fourier Neural Operator (FNO) where the output of the integral kernel is passed through a nonlinearity before the residual skip connection, following the implementation at [https://github.com/lilux618/fourier\\_neural\\_operator/blob/master/fourier\\_2d\\_time.py](https://github.com/lilux618/fourier_neural_operator/blob/master/fourier_2d_time.py), which we found to perform better. For 1D problems, we use the standard Factorized FNO (FFNO), following the implementation at <https://github.com/alasdairtran/fourierflow/>. In both cases, we make the models non-Markovian by providing the last  $K = 4$  steps as input and processing the temporal dimension as normal channels concatenated with other features, rather than as an independent dimension.

**Multi Input Galerkin Transformer (Multi Input GKT).** We use the Galerkin Transformer (GKT) implementation from <https://github.com/scaomath/galerkin-transformer>, and modify it to be non-Markovian following the same approach as in Multi-Input FNO/FFNO. Specifically, we provide the last  $K = 4$  steps as input and treat the temporal dimension as regular feature channels. We adopt the same stabilized training configuration as in Buitrago et al. [3], using a hidden size of 32, dropout of 0.05 in the attention layers, 0.025 in the feedforward layers, and training for 50 epochs.

**Factformer 2D.** As part of our evaluation, we include the original Factformer model from Li et al. [21], which is designed for spatiotemporal modeling over 2D spatial domains. While Buitrago et al. [3] only evaluated the 1D variant, we adopt the same architectural configuration for the 2D case to ensure fair comparison: four attention layers, a hidden dimension of 64, and 4 attention heads with a total projection dimension of 512. Factformer 2D applies linear attention sequentially along each spatial axis. Given a hidden tensor  $w \in \mathbb{R}^{S_x \times S_y \times H}$ , two separate MLPs ( $\text{MLP}_x$  and  $\text{MLP}_y$ ) are applied to compute keys and queries across  $S_x$  and  $S_y$ , respectively. After averaging over the complementary axis, we obtain  $q_x, k_x \in \mathbb{R}^{S_x \times H}$  and  $q_y, k_y \in \mathbb{R}^{S_y \times H}$ . Values  $v \in \mathbb{R}^{S_x \times S_y \times H}$  are computed through a shared linear projection, and attention is applied first along  $x$  and then  $y$ . Our implementation follows the original GitHub repository <https://github.com/BaratiLab/FactFormer> with minimal changes limited to data format compatibility.

**Factformer 1D.** We also evaluate the 1D version of Factformer, as introduced in Buitrago et al. [3], using the same configuration of four attention layers, hidden dimension 64, and 4 attention heads (total projection dimension 512). Unlike the 2D case, the 1D variant processes inputs over a single spatial dimension. As such, only one MLP ( $\text{MLP}_x$ ) is used to compute queries and keys, and no spatial averaging is applied. A single linear attention operation is performed per layer along the 1D spatial axis. Values are projected from the input using a linear layer. This model is implemented within the same codebase as the 2D version to maintain consistency, with minor modifications to handle 1D inputs.

**U-Net Neural Operator (U-Net).** Our U-Net implementation follows the typical encoder-decoder architecture with skip connections [10]. It consists of four downsampling convolutional blocks, a bottleneck convolutional block, and four upsampling blocks with residual connections linking corresponding encoder and decoder layers. We use a first hidden dimension of 32, and apply channel multipliers of  $[1, 2, 4, 8]$  in the encoder path. No time embeddings are used. This setup is adapted to process spatiotemporal data by flattening the spatial dimensions and independently applying the network to each time step. Our implementation is based on the publicly available codebase from PDEBench <https://github.com/pdebench/PDEBench> [27]. For reference, the U-Net Neural Operator variant used in prior work by Buitrago et al. [3] employs a similar architecture but with channel multipliers of  $[1, 2, 2, 2]$ .

## F Data Generation

### F.1 1D Burgers' Equation

We consider the one-dimensional viscous Burgers' equation, expressed as:

$$\partial_t u + u \partial_x u = \nu \partial_{xx} u, \quad (t, x) \in [0, T] \times [0, L],$$

where  $\nu$  is the viscosity coefficient. For our experiments, we utilize the publicly available 1D Burgers' dataset from PDEBench [27], with viscosity  $\nu = 0.001$ . The original dataset contains 10,000 spatiotemporal samples, each defined on a spatial grid of 1,024 points and 201 time steps over the interval  $[0, 2.01]$  seconds. We restrict our usage to the first 140 time steps and uniformly downsample them to obtain 20 steps spanning up to 1.4 seconds. This truncation is motivated by the observation that, after this point, the dissipative effect of the diffusion term  $\partial_{xx} u$  suppresses high-frequency dynamics, causing the solution to evolve slowly [3]. For training, we use the first 2,048 samples from the dataset and reserve the last 1,000 samples for testing.

### F.2 1D Kuramoto–Sivashinsky Equation

The Kuramoto–Sivashinsky (KS) equation is given by:

$$\partial_t u + u \partial_x u + \partial_{xx} u + \nu \partial_{xxx} u = 0, \quad (t, x) \in [0, T] \times [0, L],$$

with periodic boundary conditions. We follow the exact same setting as provided by Buitrago et al. [3], using their public repository at <https://github.com/r-buitrago/LPSDA>, which builds upon the implementation of Brandstetter et al. [2]. The spatial domain  $[0, 64]$  is discretized into 512 points, and the temporal domain  $[0, 2.5]$  is divided into 26 equispaced time steps with fixed  $\Delta t = 0.1$ .

Initial conditions are generated as random superpositions of sine waves:

$$u_0(x) = \sum_{i=0}^{20} A_i \sin\left(\frac{2\pi k_i}{L}x + \phi_i\right),$$

where for each trajectory, the amplitudes  $A_i$  are sampled from a continuous uniform distribution on  $[-0.5, 0.5]$ , the frequencies  $k_i$  are drawn from a discrete uniform distribution over  $\{1, 2, \dots, 8\}$ , and the phases  $\phi_i$  are sampled uniformly from  $[0, 2\pi]$ .

We consider three different viscosities:  $\nu = 0.075, 0.1$ , and  $0.125$ . For each viscosity, we generate 2,048 training samples and 256 validation samples.

### F.3 2D Navier Stokes Equations

**The TorusLi Dataset.** We consider the two-dimensional incompressible Navier–Stokes equations on the unit torus  $\mathbb{T}^2 = [0, 1]^2$  in vorticity form. The evolution of the scalar vorticity field  $\omega(x, y, t)$  is governed by:

$$\partial_t \omega + \mathbf{u} \cdot \nabla \omega = \nu \Delta \omega + f,$$

where  $\mathbf{u} = (u, v)$  is the velocity field satisfying the incompressibility condition  $\nabla \cdot \mathbf{u} = 0$ ,  $\nu > 0$  is the kinematic viscosity, and  $f$  is a fixed external forcing function.

We directly reuse the dataset released by Li et al. [20], referred to as TorusLi, which was originally developed to benchmark the FNO. The simulations were generated using a pseudospectral Crank–Nicolson second-order time-stepping scheme on a high-resolution  $256 \times 256$  grid, and subsequently downsampled to  $64 \times 64$ . All trajectories use a constant viscosity of  $\nu = 10^{-5}$  (corresponding to a Reynolds number  $\text{Re} = 2000$ ), and share the same external forcing:

$$f(x, y) = 0.1 [\sin(2\pi(x + y)) + \cos(2\pi(x + y))].$$

Initial vorticity fields  $\omega_0$  are sampled from a Gaussian random field:

$$\omega_0 \sim \mathcal{N}\left(0, 7^{3/2}(-\Delta + 49I)^{-2.5}\right),$$

with periodic boundary conditions. The numerical solver computes the velocity field by solving a Poisson equation in Fourier space and evaluates nonlinear terms in physical space with dealiasing applied. The nonlinear term is handled explicitly in the Crank–Nicolson scheme.

The dataset consists of solutions recorded every  $t = 1$  time unit, with a total of 20 time steps per trajectory, corresponding to a final time horizon of  $T = 20$ . This makes the task relatively long-range compared to other PDE benchmarks. The spatial resolution is fixed at  $64 \times 64$  for all experiments in this paper.

**The TorusVis and TorusVisForce Datasets.** We utilize two additional datasets, TorusVis and TorusVisForce, introduced by Tran et al. [28], to evaluate model generalization under varying physical regimes. Both datasets are generated using the same Crank–Nicolson pseudospectral solver used in TorusLi, maintaining consistency in numerical methodology.

These datasets extend the Navier–Stokes setting by incorporating variability in viscosity and external forcing. Specifically, each trajectory uses a randomly sampled viscosity  $\nu$  between  $10^{-5}$  and  $10^{-4}$ . The external forcing function is defined as:

$$f(t, x, y) = 0.1 \sum_{p=1}^2 \sum_{i=0}^1 \sum_{j=0}^1 [\alpha_{pij} \sin(2\pi p(ix + jy) + \delta t) + \beta_{pij} \cos(2\pi p(ix + jy) + \delta t)],$$

where  $\alpha_{pij}, \beta_{pij} \sim \mathcal{U}[0, 1]$  are sampled independently for each trajectory. The parameter  $\delta$  controls the temporal variation in the forcing: for TorusVis,  $\delta = 0$ , resulting in time-invariant forcing; for TorusVisForce,  $\delta = 0.2$ , producing a time-varying force.

As with TorusLi, the spatial resolution is fixed at  $64 \times 64$ , and trajectories consist of 20 time steps sampled every  $t = 1$  time unit, yielding a total time horizon of  $T = 20$ .



## G Normalization Strategy for 1D Burgers’ Equation

Prior studies, such as Tran et al. [28] and Buitrago et al. [3], employ a specific normalization strategy likely based on the implementation in the official `fourierflow` repository <https://github.com/aldasairtran/fourierflow>, combined with a lower number of training epochs.

In our experiments, we normalize the data to the  $[0, 1]$  range and train each model for 500 epochs. We find that the normalization strategy has a significant effect on model performance, whereas increasing the number of training epochs has little to no consistent impact.

For fair comparison, we also evaluate our model using the normalization method adopted by Buitrago et al. [3], without modifying our default hidden dimension or architecture. Note that their FFNO uses  $2\times$  the hidden size and  $4\times$  the linear expansion size compared to our model. Additionally, our ST-SSM uses a fixed memory window of  $K = 4$ , whereas their models access the full sequence history. We omit comparisons on GKT due to fundamental architectural differences: they employ a Markovian variant, while we use a multi-input version.

Interestingly, we observe that FFNO and other baselines benefit significantly from the  $[0, 1]$  normalization scheme, even with smaller model sizes. As a result, we adopt this setup throughout the paper and refrain from further analysis of normalization schemes, which we consider outside the current scope.

Table 6: Comparison of relative  $\mathcal{L}^2$  error on 1D Burgers’ Equation using different normalization and training setups. Our setup uses data normalization to  $[0, 1]$  and 500 training epochs, while Buitrago et al. [3] use their original configuration.

Architecture	Relative $\mathcal{L}^2$ Error	
	Ours	Results from Buitrago et al. [3]
U-Net	0.067	0.112
Factformer (1D)	0.015	0.117
FFNO	0.020	0.099
Multi Input FFNO	0.016	0.028
S4-FFNO	0.016	0.030
ST-SSM	<b>0.007</b>	<b>0.018</b>

## H Pseudocode for 2D ST-SSM Architecture

```
class STSSM(nn.Module):
    """
    Notation:
        B: batch size
        T: temporal length
        X, Y: spatial dimensions
        C: input channels
        H: hidden dimension
    """

    def __init__(self,
        lifting_layer: nn.Module,
        projection_layer: nn.Module,
        memory_pre_forward_x: nn.Module,
        memory_pre_backward_x: nn.Module,
        memory_pre_forward_y: nn.Module,
        memory_pre_backward_y: nn.Module,
        memory_t: nn.Module,
        memory_post_forward_x: nn.Module,
        memory_post_backward_x: nn.Module,
        memory_post_forward_y: nn.Module,
        memory_post_backward_y: nn.Module):
        super().__init__()
        self.p = lifting_layer
        self.q = projection_layer
        self.memory_pre_forward_x = memory_pre_forward_x
        self.memory_pre_backward_x = memory_pre_backward_x
        self.memory_pre_forward_y = memory_pre_forward_y
        self.memory_pre_backward_y = memory_pre_backward_y
        self.memory_t = memory_t
        self.memory_post_forward_x = memory_post_forward_x
        self.memory_post_backward_x = memory_post_backward_x
        self.memory_post_forward_y = memory_post_forward_y
        self.memory_post_backward_y = memory_post_backward_y

    def forward(self, x: Tensor) -> Tensor:
        """
        Args:
            x: Input sequence of states (B, C, X, Y, T)
        Returns:
            Predicted next state (B, X, Y, 1)
        """

        if self.training:
            x = x + torch.randn_like(x) * noise

        x = rearrange(x, 'b c x y t -> (b t) x y c')
        x = self.p(x)
        x = rearrange(x, '(b t) x y h -> (b t) h x y', t=T)

        # --- Pre-memory spatial SSM ---
        x = rearrange(x, '(b t) h x y -> (b t y) h x', t=T)
        x_fwd = self.memory_pre_forward_x(x)[0]
        x_bwd = torch.flip(self.memory_pre_backward_x(torch.flip(x, dims
            =[-1]))[0], dims=[-1])
        x = x_fwd + x_bwd
        x = rearrange(x, '(b t y) h x -> (b t) x h y', t=T)

        x = rearrange(x, '(b t) x h y -> (b t x) h y', t=T)
        y_fwd = self.memory_pre_forward_y(x)[0]
        y_bwd = torch.flip(self.memory_pre_backward_y(torch.flip(x, dims
            =[-1]))[0], dims=[-1])
```

```

x = y_fwd + y_bwd
x = rearrange(x, '(b t x) h y -> (b t) h x y', t=T)

# --- Temporal SSM ---
x = rearrange(x, '(b t) h x y -> b x y h t', t=T)
x = rearrange(x, 'b x y h t -> (b x y) h t')
x = self.memory_t(x)[0]
x = rearrange(x, '(b x y) h t -> b x y h t', x=X, y=Y)
x = rearrange(x, 'b x y h t -> (b t) h x y', t=T)

# --- Post-memory spatial SSM ---
x = rearrange(x, '(b t) h x y -> (b t y) h x', t=T)
x_fwd = self.memory_post_forward_x(x)[0]
x_bwd = torch.flip(self.memory_post_backward_x(torch.flip(x, dims
=[-1]))[0], dims=[-1])
x = x_fwd + x_bwd
x = rearrange(x, '(b t y) h x -> (b t) x h y', t=T)

x = rearrange(x, '(b t) x h y -> (b t x) h y', t=T)
y_fwd = self.memory_post_forward_y(x)[0]
y_bwd = torch.flip(self.memory_post_backward_y(torch.flip(x, dims
=[-1]))[0], dims=[-1])
x = y_fwd + y_bwd
x = rearrange(x, '(b t x) h y -> (b t) h x y', t=T)

x = self.q(x)
x = rearrange(x, '(b t) c x y -> b x y t c', t=T)

return x

```

Listing 3: ST-SSM pseudocode